arXiv:astro-ph/0612705v1 22 Dec 2006

# Proper Motions of Dwarf Spheroidal Galaxies from *Hubble Space Telescope* Imaging. V: Final Measurement for Fornax.[1]

Slawomir Piatek

*Dept. of Physics, New Jersey Institute of Technology, Newark, NJ 07102*
*E-mail address: piatek@physics.rutgers.edu*

Carlton Pryor

*Dept. of Physics and Astronomy, Rutgers, the State University of New Jersey, 136 Frelinghuysen Rd., Piscataway, NJ 08854–8019*
*E-mail address: pryor@physics.rutgers.edu*

Paul Bristow

*Instrument Division, European Southern Observatory, Karl-Schwarzschild-Str. 2, D-85748, Garching bei Munchen, Germany*
*E-mail address: Paul.Bristow@eso.org*

Edward W. Olszewski

*Steward Observatory, University of Arizona, Tucson, AZ 85721*
*E-mail address: eolszewski@as.arizona.edu*

Hugh C. Harris

*US Naval Observatory, Flagstaff Station, P. O. Box 1149, Flagstaff, AZ 86002-1149*
*E-mail address: hch@nofs.navy.mil*

Mario Mateo

*Dept. of Astronomy, University of Michigan, 830 Denninson Building, Ann Arbor, MI 48109-1090*
*E-mail address: mmateo@umich.edu*

Dante Minniti

*Universidad Catolica de Chile, Department of Astronomy and Astrophysics, Casilla 306, Santiago 22, Chile*
*E-mail address: dante@astro.puc.cl*

Christopher G. Tinney

*Anglo-Australian Observatory, PO Box 296, Epping, 1710, Australia*
*E-mail address: cgt@aao.gov.au*

## ABSTRACT

The measured proper motion of Fornax, expressed in the equatorial coordinate system, is $(\mu_\alpha, \mu_\delta) = (47.6 \pm 4.6, -36.0 \pm 4.1)$ mas century$^{-1}$. This proper motion is a weighted mean of four independent measurements for three distinct fields. Each measurement uses a quasi-stellar object as a reference point. Removing the contribution of the motion of the Sun and of the Local Standard of Rest to the measured proper motion produces a Galactic rest-frame proper motion

of $(\mu_\alpha^{\rm Grf}, \mu_\delta^{\rm Grf}) = (24.4 \pm 4.6, -14.3 \pm 4.1)$ mas century$^{-1}$. The implied space velocity with respect to the Galactic center has a radial component of $V_r = -31.8 \pm 1.7$ km s$^{-1}$ and a tangential component of $V_t = 196 \pm 29$ km s$^{-1}$. Integrating the motion of Fornax in a realistic potential for the Milky Way produces orbital elements. The perigalacticon and apogalacticon are 118 (66, 137) kpc and 152 (144, 242) kpc, respectively, where the values in the parentheses represent the 95% confidence intervals derived from Monte Carlo experiments. The eccentricity of the orbit is 0.13 (0.11, 0.38), and the orbital period is 3.2 (2.5, 4.6) Gyr. The orbit is retrograde and inclined by 101° (94°, 107°) to the Galactic plane. Fornax could be a member of a proposed "stream" of galaxies and globular clusters, however the membership of another proposed galaxy in the stream, Sculptor, has been previously ruled out. Fornax is in the Kroupa-Theis-Boily plane that contains eleven of the Galactic satellite galaxies, but its orbit will take it out of that plane.

*Subject headings:* galaxies: dwarf spheroidal — galaxies: individual (Fornax) — astrometry: proper motion

## 1. Introduction

The Local Group is a dynamic environment. Galaxies swarm in the gravitational well of the cluster and move about each other. The Earth-bound observer had only a one-dimensional view of this plethora of motions until a few decades ago: measuring the radial components of velocities was "easy," measuring the tangential components was hard. Most of the difficulty lies in measuring the proper motion of a galaxy — which must be done with respect to cosmic standards of rest, such as high-redshift galaxies and quasi-stellar objects (QSOs). Since the size of a proper motion decreases with increasing distance, all else being equal, measuring motions of even the nearest galaxies required time baselines of several tens of years using images taken with the ground-based telescopes or just years when using those taken with the Hubble Space Telescope (HST).

The analysis of the astrometric data is complex. The available ground-based images were acquired with a variety of telescopes and imagers and under different atmospheric conditions and air masses and, thus, they contain non-uniform distortions. Understanding and characterizing these distortions is essential because the expected measured proper motion is very small — on the order of a few tens of mas century$^{-1}$. Although space-based data do not contain distortions caused by the atmosphere, the analysis of such data is still complicated because of several factors. 1. Useful reference points are scarce. Even bright and compact background galaxies have larger positional uncertainties than star-like objects. The field of view of *HST* is small, thus, a typical image contains too few such galaxies to serve as useful standards of rest. Instead, a QSO with its star-like point-spread function (PSF) is the standard of rest of choice. Therefore, the availability of QSOs within the appropriate brightness range behind the target galaxy determines the number of independent images — fields. 2. Stars are scarce, ranging in number from a few tens to a few hundreds per field. This scarcity limits the ability to measure the PSF, to transform stellar coordinates between epochs, and to determine the average proper motion of the galaxy. 3. The images still contain distortions that are inherent to the detectors and optics of *HST*. The expected motion of stars with respect to the QSO is on the order of a few thousandth of a pixel in several years, therefore, a model for these distortions should be

[1]Based on observations with NASA/ESA *Hubble Space Telescope*, obtained at the Space Telescope Science Institute, which is operated by the Association of Universities for Research in Astronomy, Inc., under NASA contract NAS 5-26555.

accurate to a sub-pixel scale. None of the existing models has such accuracy. Despite these obstacles, clever observations and data analysis have allowed the list of nearby galaxies with a measured proper motion to grow steadily.

In alphabetical order, the list now contains: Draco (Scholtz & Irwin 1993), Canis Major (Dinescu et al. 2005b), Carina (Piatek et al. 2003), Fornax (Piatek et al. 2002; Dinescu et al. 2004), LMC (Jones et al. 1994; Kroupa et al. 1994; Kroupa & Bastian 1997; Anguita et al. 2000; Drake et al. 2001; Pedreros et al. 2002; Kallivayalil et al. 2006a), M33 (Brunthaler et al. 2005), Sagittarius (Dinescu et al. 2005a), Sculptor (Schweitzer et al. 1995; Piatek et al. 2006), SMC (Irwin et al. 1996; Kallivayalil et al. 2006b), and Ursa Minor (Scholtz & Irwin 1993; Schweitzer et al. 1997; Piatek et al. 2005). This sample is becoming large enough to reveal the three-dimensional nature of motions in the Local Group. Notable is the measurement for M33, the Triangulum Galaxy, the third most luminous galaxy in the Local Group at a distance from the Milky Way comparable to that for M31. Brunthaler et al. (2005) use radio observations with the Very Long Baseline Array of two groups of water masers located on opposite sides of the galaxy to derive a proper motion on the order of 50 $\mu$as yr$^{-1}$. This is the smallest proper motion of a galaxy ever measured. The uncertainties in the model of the rotation of M33 and not measurement errors dominate the uncertainty of this proper motion.

Just as the motions of planets around the Sun contain information about the mass distribution in and the formation of the Solar System, space velocities of galaxies contain such information for the Local Group. In addition, the space velocities give galactic orbits, and these can demonstrate if the galaxies evolved in seclusion or if they influenced each other through close encounters, collisions, or mergers.

Dark matter continues to evade direct detection. Its gravitational interaction with the luminous matter and light is the key observational clue for its existence. On a galactic scale, the rotation curve of a spiral galaxy or the velocity dispersion profile of an elliptical galaxy are such key observations, whereas, on the scale of galaxy groups, it is the velocity dispersion of the member galaxies. Knowing all three components of the space velocities of the galaxies provides a check on the assumption of velocity isotropy in the mass estimates based on the velocity dispersion. It also offers additional ways of constraining the amount and distribution of dark matter. For example, for the Milky Way and its satellite dwarf galaxies one may: 1. Derive a lower limit for the mass of the Milky Way from the assumption that a satellite galaxy is bound or derive an estimate of the mass of the Milky Way out to the radius of the satellites from their velocity dispersion. 2. Derive a limit on the amount of dark matter in a satellite galaxy that approaches the Milky Way closely enough that the Galactic tidal force is significant compared to the self-gravity of the galaxy.

The space velocities of galaxies can also test more general features of models for a cold dark matter cosmology by: 1. Comparing the distributions of the observed orbital elements with those predicted by numerical simulations of the formation of the Local Group (Gill et al. 2004; Moore et al. 2006). 2. Investigating possible close encounters and collisions among the satellite galaxies (Zhao 1998; Dinescu et al. 2004).

Two interesting ideas about the formation of the satellite galaxies of the Milky Way challenge the picture that these galaxies are surviving substructure, predicted by cold dark matter cosmology. Lynden-Bell & Lynden-Bell (1995) propose that some Galactic satellite galaxies and globular clusters move along similar orbits — they are members of a "stream" formed when the tidal force of the Milky Way tore a progenitor satellite galaxy into fragments. The fragments continue to move together on the orbit of the progenitor in the absence of collisions, significant orbital precession, or dynamical friction. This is a testable idea: Lynden-Bell & Lynden-Bell (1995) predict proper motions for the members of proposed streams. The other testable idea is based on the "planar" distribution of the Galactic dwarf galaxies. Kroupa et al. (2005) note that the 11 galaxies

nearest to the Milky Way lie within a disk whose thickness-to-radius ratio is $\leq 0.15$. Kroupa et al. (2005) argue that such a distribution of satellites is very unlikely for the substructure predicted by cold dark matter cosmologies, though this is disputed by Libeskind et al. (2005) and Zentner et al. (2005). If the orbits of the satellites are indeed within the disk, the geometry of the plane predicts the coordinates of their poles. Note that the galaxies do not have to share the same orbit — be in a stream — for their orbital poles to be the same, all that is required is that their orbits must be in the same plane.

This article is one of a series that is attempting to better-define the kinematics of the Local Group and reports a measurement of the proper motion for the Fornax dSph galaxy. The measurement derives from a larger set of data than and, thus, replaces the preliminary measurement reported in Piatek et al. (2002). Section 2 presents Fornax, emphasizing those of its physical and structural properties that are relevant to our analysis. Section 3 describes the observations and data and Section 4 explains the process of deriving the proper motion making use of several key performance diagnostics. The next three sections, §5, §6, and §7, present the measured proper motion and space velocity, calculate the implied Galactic orbit, and discuss the implications of the motion, respectively. The final section, §8, is a summary.

## 2. Physical and Structural Properties of Fornax

Among the Galactic dSphs, Fornax is one of the "giants." The luminosity of Fornax, given in Table 1, is comparable to that of Sagittarius, at least three times greater than that of the next most luminous dSph, Leo I, and about two orders of magnitude greater than that of the least luminous — Draco. Fornax and Sgr are the only dSphs with confirmed globular clusters. Reviews of research on dwarf galaxies in the Local Group by Mateo (1998) and van den Bergh (2000), and a study of structure of the Galactic dSphs by Irwin & Hatzidimitriou (1995) are convenient sources for a side-by-side comparison of the dSphs.

Discovered by Shapley (Shapley 1938a,b), Fornax is at the celestial location $(\alpha, \delta) = (02^{\rm h}39^{\rm m}53\overset{\rm s}{.}1, -34°30'16.0'')$ (van den Bergh 1999) in the J2000.00 equatorial coordinate system. This location corresponds to $(\ell, b) = (237.245°, -65.663°)$ in the Galactic coordinate system. The galaxy is only about 21° on the sky from the Sculptor dSph.

Saviane et al. (2000) derived a distance modulus of $(m - M)_0 = 20.70 \pm 0.12$ for Fornax using the magnitude of the tip of the red giant branch. The data consist of ground-based observations in the $B$, $V$, and $I$ bands of four overlapping fields, each with an effective area of $10.7' \times 10.7'$. The implied heliocentric distance is $138 \pm 8$ kpc. Our study adopts this distance when calculating distance-dependent quantities. An earlier measurement of the distance modulus by Buonanno et al. (1999), using archival *HST* photometry in the F555W and F814W bands of cluster 4 in Fornax and its surroundings, produced a similar value.

Several studies have investigated the structure of Fornax using wide-field imaging. A "benchmark" investigation is that by Irwin & Hatzidimitriou (1995), who used star counts from a photographic plate taken with UK Schmidt telescope to derive the key structural parameters. Their field of view is about 36 deg$^2$. In a similar manner, the study also derives structural parameters for seven other dSphs. Table 1 lists the values for the ellipticity, position angle, and core and tidal radii from Irwin & Hatzidimitriou (1995). This contribution adopts these values where they are needed.

An analysis of deeper images, albeit with smaller areal coverage, by Walcher et al. (2003) produces a similar set of structural parameters as that in Irwin & Hatzidimitriou (1995). The images cover an area of 8.5 deg$^2$ and reach a limiting magnitude of 23.5 in the $V$ band. The resulting isopleth map shows a steeper

decline in the projected surface density on the south and east sides of the galaxy *versus* the north and west sides — a behavior noted previously by several studies, for example, Demers et al. (1994) or Stetson et al. (1998).

More recently, Coleman et al. (2005) surveyed Fornax producing images with a total areal coverage of 10 deg$^2$ in the $V$ and $I$ bands and reaching a limiting magnitude $V = 20$. The surface density of stars selected to lie along the giant branch shows that: 1) stars beyond the Irwin & Hatzidimitriou (1995) tidal radius are found to the north-west and south-east of the galaxy, which is the orientation of the minor axis and 2) there is an additional overdensity of stars in a shell about 1.3° to the north-west of the galaxy. Coleman et al. (2004) argued that the asymmetry in the surface density profile noted in the previous paragraph is caused by another shell about 17′ to the south-east and that this feature is dominated by a stellar population with an age of about 2 Gyrs. Coleman et al. (2005) propose that these two shells and the other extra-tidal stars are the signature of the infall of a gas-rich galaxy with $M_V \simeq -8$. Deeper imaging by Olszewski et al. (2006) confirms that the inner shell contains an excess of stars formed in a burst about 1.4 Gyr ago. The location of these stars in the color-magnitude diagram indicates that they have [Fe/H]$= -0.7$, which is higher than that expected for a low-luminosity dwarf galaxy and implies that these stars formed from enriched gas originating from Fornax. The conflict between the evidence for infall — shells and extratidal stars — and the high metallicity of the inner shell may perhaps be resolved by star formation stimulated by a minor merger.

Mateo et al. (1991) measured radial velocities for 44 stars in two fields located in the direction of Fornax. One field coincides with the center of the galaxy and the other is about two core radii away from the center in the south-west direction. After excluding 12 likely non-member stars from the sample, the measured radial velocities imply a heliocentric systemic velocity of $53 \pm 1.8$ km s$^{-1}$. The sample shows no evidence for a significant rotation around the minor axis. The velocity dispersion is $9.9 \pm 1.7$ km s$^{-1}$ in the central field and $12.0 \pm 2.8$ km s$^{-1}$ in the outer — thus, the velocity dispersion does not vary significantly with the projected radius. The study derives a mass-to-light ratio ($M/L_V$) of $12.3 \pm 4.5$ in solar units for the center of Fornax, but notes that $M/L_V$s in the range between 5.3 and 26 are also acceptable given the uncertainties in the fitted structural parameters. More recently, Walker et al. (2006) measured radial velocities for an additional 176 stars scattered throughout the galaxy and combined these measurements with those in Mateo et al. (1991) in their analysis. The combined sample with the most stringent exclusion of non-members implies $53.3 \pm 0.8$ km s$^{-1}$ for the heliocentric radial velocity, which our contribution adopts when calculating quantities that depend on this parameter. The global velocity dispersion is $11.6 \pm 0.6$ km s$^{-1}$; the velocity dispersion calculated in radial bins does not vary with projected radius.

Piatek et al. (2002) and Dinescu et al. (2004) independently measured the proper motion of Fornax. The measurement by Piatek et al. (2002) of $(\mu_\alpha, \mu_\delta) = (49 \pm 13, -59 \pm 13)$ mas century$^{-1}$ derives from *HST* images of three distinct fields using STIS or WFPC2. For two of these fields, the data are at two epochs separated by 1 - 2 years. For the third field, the data are at three epochs with a total time baseline of 2 years. The measurement of Piatek et al. (2002) is preliminary because it was based on partial data while the observing program was still ongoing. The measurement quoted in this contribution, which derives from the complete set of data, replaces the older preliminary measurement. The measurement by Dinescu et al. (2004) of $(\mu_\alpha, \mu_\delta) = (59 \pm 16, -15 \pm 16)$ mas century$^{-1}$ derives from a combination of ground-based and *HST* imaging. The time baseline between epochs varies between 20 and 50 years. Some of the space-based data are the same as those in Piatek et al. (2002), but they are such a tiny fraction of the whole dataset that the measurement in Dinescu et al. (2004) can be considered independent from that in Piatek et al. (2002) or this article.

## 3. Observations and Data

The data consist of images taken with *HST* in three distinct fields in the direction of Fornax. Each field contains at least one known QSO. Figure 1 shows the configuration of the fields — each represented by a square — on a $60' \times 60'$ section of the sky. The center of Fornax is at $(X, Y) = (0', 0')$. North is up and East is to the left. The dashed ellipse in the figure represents the core. Its semi-major axis, ellipticity, and position angle are those in Table 1. One of the three fields — the smallest in size — is within the core and

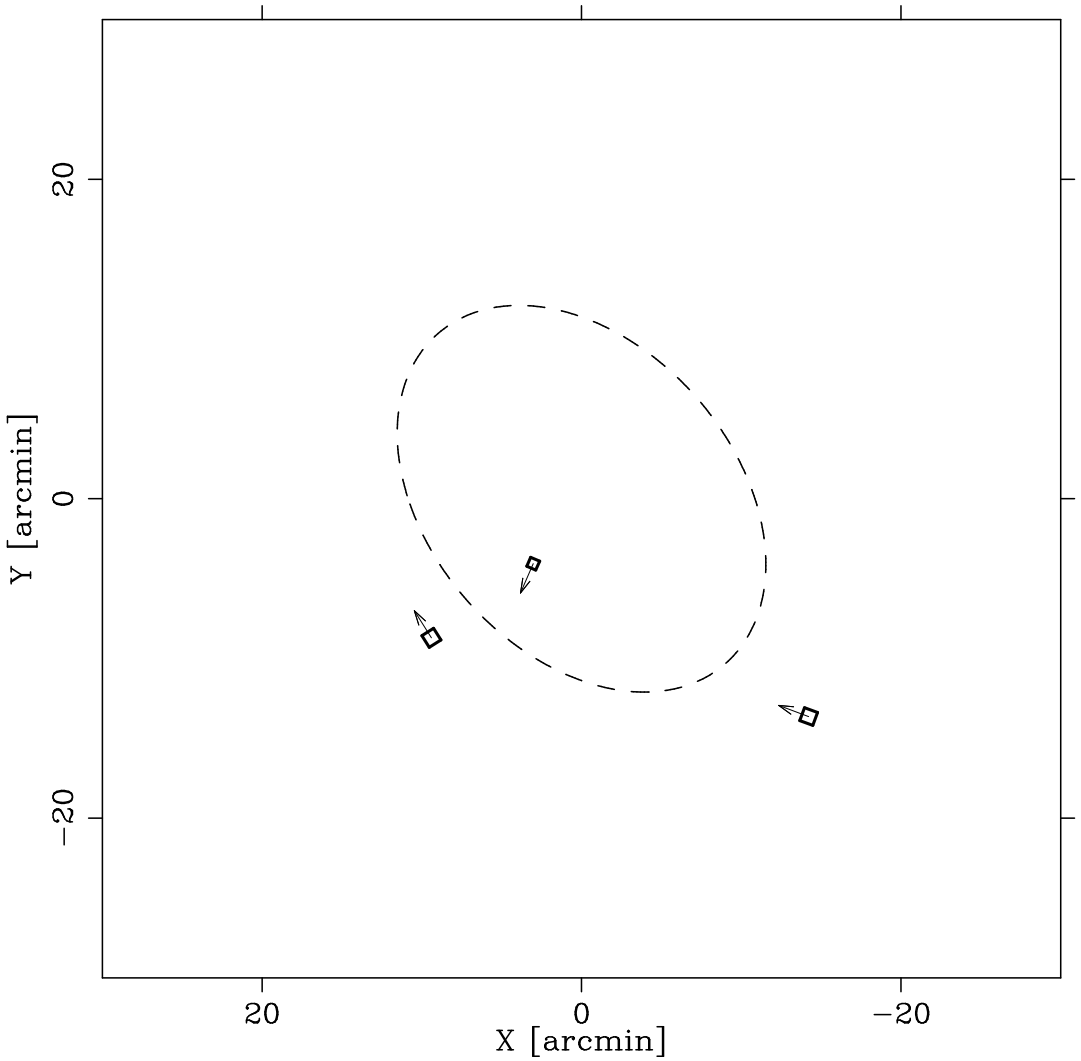


Fig. 1.— A $60' \times 60'$ section of the sky in the direction of Fornax. North is up and East is to the left. The dashed ellipse represents the measured core. The three squares depict the fields that this article studies. From North to South, they correspond to the fields FOR J0238 − 3443, FOR J0240 − 3434, and FOR J0240 − 3438. An arrow indicates the direction of the positive $Y$ axis of the CCD.

close to the minor axis. An arrow emanating from a field points in the direction of the positive $Y$ axis in the CCD. The name of each field and the equatorial coordinates of its center are in the first three columns of Table 2.

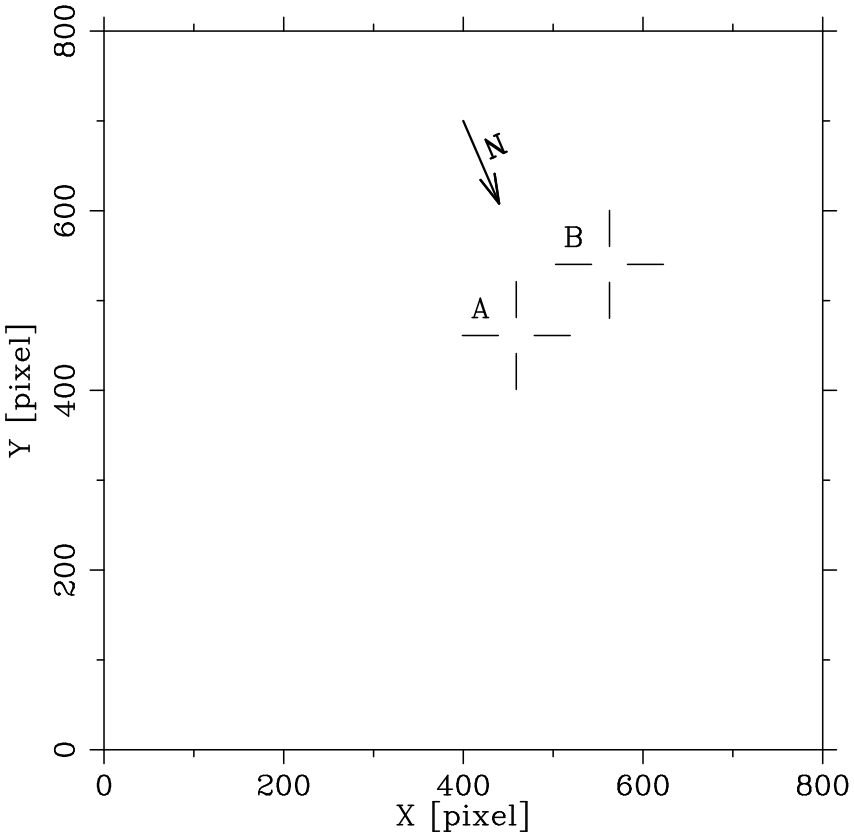


Fig. 2.— A sample image from the epoch 1999 data for the FOR J0240 − 3434 field. It is an average of two images at one dither position with cosmic rays removed. Each image of the lensed QSO lies within a cross-hair. North is in the direction indicated by an arrow and east is 90° counter-clockwise from north.

The most northern field is FOR J0240 − 3434. It is approximately centered on image A of a lensed QSO discovered by Tinney (1995) and located at $(\alpha, \delta) = (02^{\rm h}40^{\rm m}07\overset{\rm s}{.}73, -34°34'19.8'')$ (Yentis et al. 1992). Image B of the QSO is 6.1″ away from image A. Tinney (1995) measured the $B$-band magnitude and $B - H$ color of image A to be $19.00 \pm 0.05$ and $1.42 \pm 0.08$, respectively, and of image B to be $19.77 \pm 0.05$ and $1.92 \pm 0.08$, respectively. The redshift of the QSO measured from both images is 1.4.

HST observed the FOR J0240 − 3434 field on March 10, 1999; March 8, 2001; and March 8, 2003 using the Planetary Camera (PC2) of the Wide Field and Planetary Camera 2 (WFPC2) and the F606W filter (columns 4 — 6 of Table 2). The observations produced 18, 16, and 16 images, respectively, each with an exposure time of 160 s (column 7 of Table 2). The position angle of 156.6° for the Y axis of the CCD is the same to within 0.01° for all of the exposures. Figure 2 is a sample image from the 1999 epoch.

The other two fields shown in Figure 1 are, in order of decreasing declination FOR J0240 − 3438 and FOR J0238 − 3443. Again, each field contains and is approximately centered on a known QSO. Tinney et al. (1997) provide information on these QSOs. The QSO in the FOR J0240 − 3438 field is at $(\alpha, \delta) = (02^{\rm h}40^{\rm m}38\overset{\rm s}{.}7, -34°38'58'')$ (J2000.0), has a $B$-band magnitude of 20.2, and a redshift of 0.38. The QSO in the FOR J0238 − 3443 field is at $(\alpha, \delta) = (02^{\rm h}38^{\rm m}43\overset{\rm s}{.}8, -34°43'53'')$ (J2000.0), has a $B$-band magnitude of 20.2, and a redshift of 2.0.

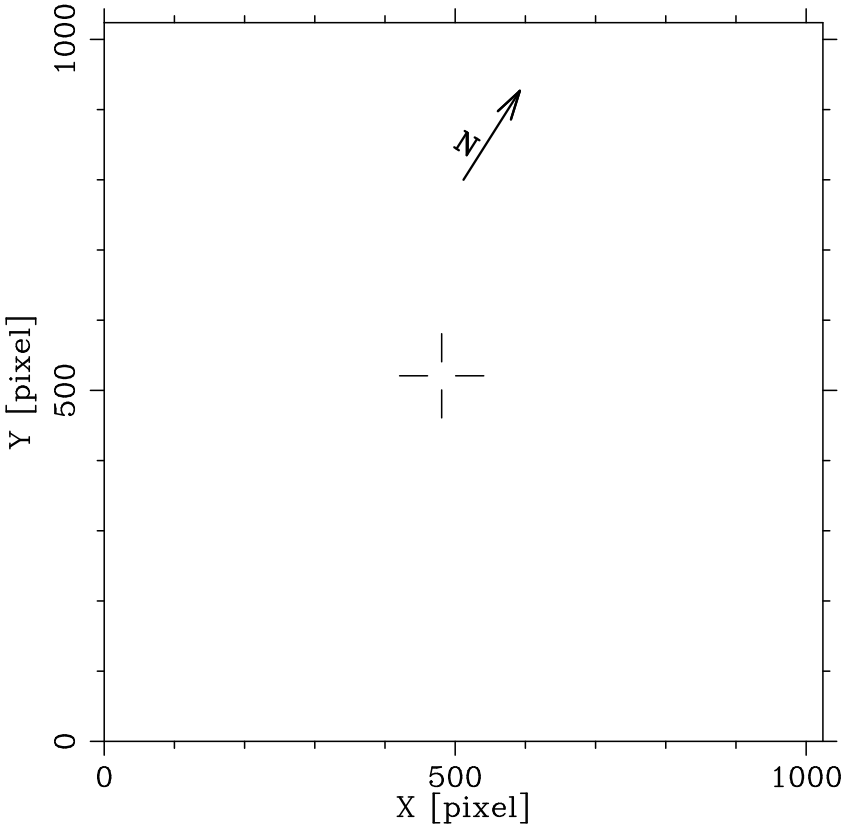


Fig. 3.— A sample image from the epoch 2000 data for the FOR J0240 − 3438 field. It is a sum of three images at one dither position with cosmic rays removed. The cross-hair indicates the QSO.

HST observed the FOR J0240 − 3438 field on January 31, 2000; January 25, 2001; and January 29, 2002. It observed the FOR J0238 − 3443 field on March 8, 2000; March 8, 2001; and March 9, 2003. For all of these observations, HST used the Space Telescope Imaging Spectrograph (STIS) with no filter (50CCD). There are 24 images per epoch of the FOR J0240 − 3438 field, each with an exposure time of 192 s, for a total of 72 images. The position angle of the Y axis for all of the images is 32.4° to within 0.05°. There are also 24 images per epoch in the FOR J0238 − 3443 field for a total of 72 images. The average exposure times at the three epochs are 193 s, 192 s, and 189 s, respectively, and the position angle of the Y axis is 69.7° to within 0.06°. Table 2 summarizes the above information. Figures 3 and 4 are sample images from the earliest observations in the two fields.

### 3.1. Charge Transfer Efficiency

During the readout of a CCD, the electrical charge present in a pixel at the end of an exposure transfers from pixel to pixel towards the transfer register. For STIS, this motion is in the positive $Y$ direction, or "up," whereas for PC2, it is in the negative, or "down," direction. Once in the transfer register, the charge moves along the $X$ direction to the circuit that measures its amount. The transfer of the charge is imperfect: CCD pixels contain "charge traps" which both capture and release charge. Thus, the quantity of charge passing

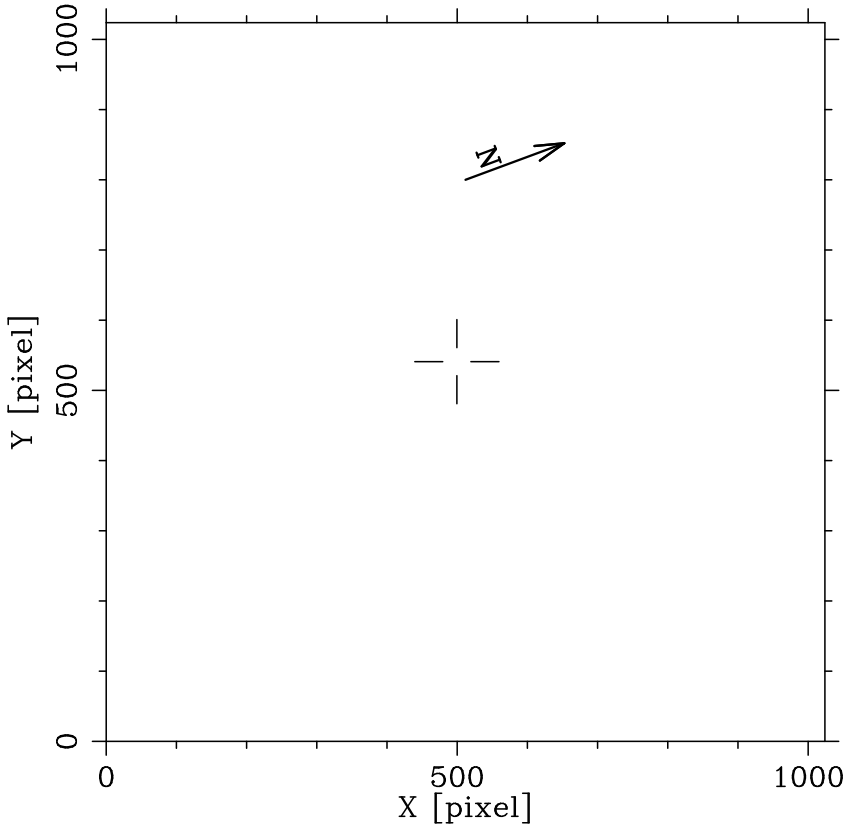


Fig. 4.— A sample image from the epoch 2000 data for the FOR J0238 − 3443 field. It is a sum of three images at one dither position with cosmic rays removed. The cross-hair indicates the QSO.

through a pixel can either increase, if more charge is captured than released, or decrease, if the reverse is true. Because the charge traps have a finite capacity, they have a smaller fractional effect on bright sources than on faint sources. The origin of charge traps is not completely understood, but it is known that the efficiency of charge transfer in STIS and WFPC2 decreases with time (Whitmore et al. 1999; Goudfrooij et al. 2006) — most likely because of defects in the crystal lattice of the CCD created by cosmic radiation (Janesick et al. 1991). Therefore, the effect of charge traps on the photometry and astrometry increases with time.

Bristow et al. (2005) describe the various effects caused by charge traps and why these effects arise, emphasizing the impact on time-dependent astrometry such as the measurement of a proper motion. Figure 5 illustrates how charge traps can create a spurious proper motion. Consider a field that contains three stars with similar signal values and a QSO with a much larger signal. In the figure, the stars and the QSO are represented by open circles and a solid square, respectively, and are labeled as $S1$, $S2$, $S3$, and $Q$. The QSO is the reference point. Assume that the stars, the QSO, and the observer are at rest with respect to each other, which means that the observer should detect no motion for any star with respect to the QSO. Figure 5 depicts two hypothetical images of this field taken at $t = 0$ and at $t = T$ with exactly the same pointings of the telescope and with a CCD that contains charge traps whose number has increased with time. Let the measured centroid of a source be depicted by the location of the source in an image. Because in the time interval $T$ separating the two images the number of charge traps has increased, a centroid in the later image has a smaller value of $Y$ — it has shifted away from the transfer register. Here we ignore

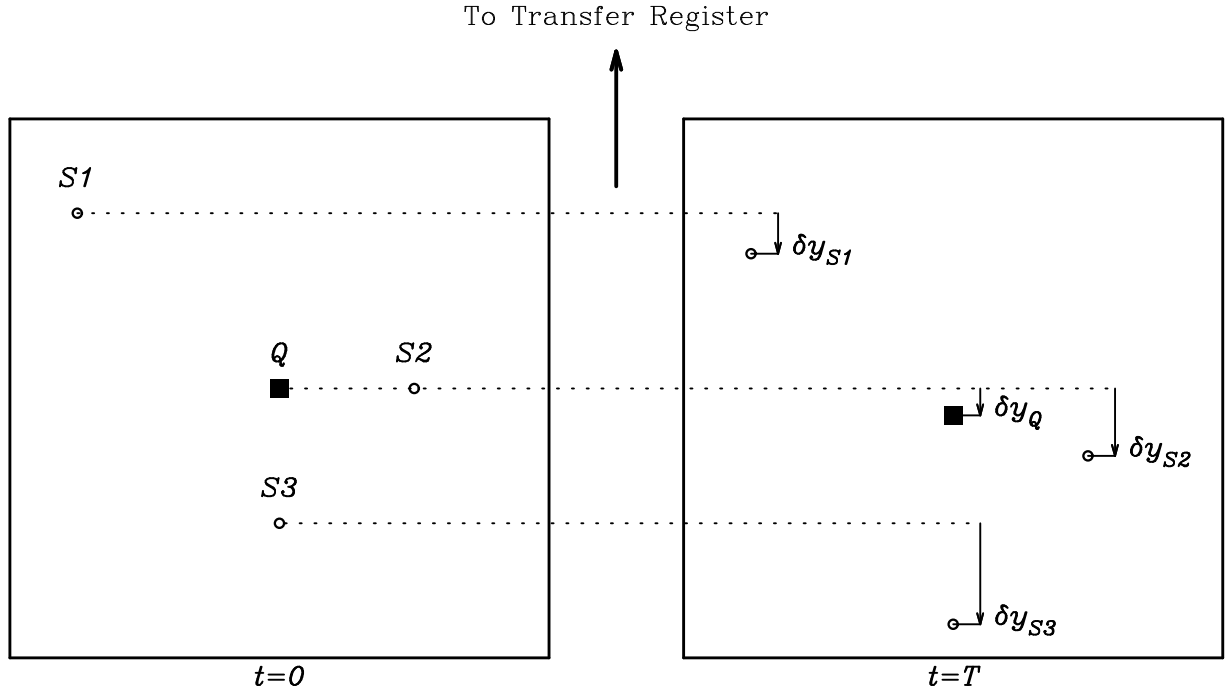


Fig. 5.— Hypothetical images taken at $t = 0$ (left) and at $t = T$ (right) with a CCD containing charge traps whose number increases with time. There are four sources in an image: three stars and a QSO. The open circles, labeled $S1$, $S2$, and $S3$, represent the three stars while the solid square, labeled $Q$, represents the QSO. The location depicted for a source in an image corresponds to its measured centroid. The signal in the QSO is much larger than the signal in each star, the latter assumed to be about the same. Because the number of charge traps has increased between $t = 0$ and $t = T$, a measured centroid in the "later" image has a smaller value of $Y$, that is, the centroid has shifted in the direction of decreasing $Y$ values. Arrows in the figure represent these shifts. The magnitude of the shift depends on the location of a source in the image and on its signal.

a possible shift in the $X$ direction resulting from inefficient charge transfer in the serial register since this inefficiency is negligible for STIS (Brown et al. 2002) and one-third as large as in the parallel direction for WFPC2 (Heyer et al. 2004). The arrows $\delta y_Q, \delta y_{S1}, \delta y_{S2}$, and $\delta y_{S3}$ represent these shifts for the QSO and the three stars, respectively. The magnitude of the shift is larger the smaller the signal of the object and the greater its distance from the serial register. Thus, for example, $S3$ has a spurious motion in the coordinate system of the CCD of $(\delta y_{S3} - \delta y_Q)/T$, which implies that the observer would measure a proper motion for $S3$ with respect to the QSO.

Both WFPC2 and STIS contain charge traps whose number increases with time as a consequence of the ongoing production of lattice defects by the cosmic radiation (Janesick et al. 1991). The transfer register is at the bottom of the image for PC2 and at the top for STIS. Therefore, the centroids shift towards larger values of $Y$, or "up," for PC2 and towards smaller values of $Y$, or "down," for STIS. Accurate astrometry requires either that the shifts are accounted for in the analysis or that a CCD image be "restored" so that its pixels have the same values as immediately before the readout. Bristow & Alexov (2002) developed a software package that restores an image taken with STIS, which was used to correct all of our images taken with STIS prior to our analysis. No corresponding software exists for restoring an image taken with PC2. In this case, our analysis measures and removes the shifts — the details are in Section 5.1.

To estimate how greatly the decreasing charge transfer efficiency can affect the measured proper motion, this study performs a parallel analysis ignoring the effects of charge traps and comments on the difference.

## 4. Measuring Proper Motion

Piatek et al. (2006) and references therein describe our method of deriving a proper motion from undersampled images taken with *HST*. This article outlines briefly the four major components of the method.

1. Determine the initial estimates for the centroids of objects — stars and the QSOs. This task uses stand-alone astronomy software packages such as DAOPHOT, ALLSTAR, and DAOMASTER (Stetson 1987, 1992, 1994). For each field and epoch, this step produces a list of objects at that epoch and the translational offsets between the chronologically first image of an epoch — the fiducial image — and those that follow. The centroid of an object on the list is in the coordinate system of the fiducial image; however, its centroid in any other image derives from the known offsets.

2. Construct an effective point-spread function (ePSF; Anderson & King (2000)) for each field and epoch. Using a select set of stars and the QSOs, our method builds a single, position-independent or constant ePSF that is used for all of the images of a field at an epoch. An object contributes to the construction of the ePSF if its signal-to-noise ratio (S/N) is greater than some limit — 15 for these data — and if its inner $3 \times 3$ array of pixels (see Piatek et al. (2002) for details about the structure of the data) have data quality flags equal to 0. If there are $N$ images for a given field and epoch, an object may contribute up to $N$ times to the construction of the ePSF — fewer if the object is flagged out in some images.

3. Derive accurate centroids for objects by fitting an ePSF to the image of each object using least squares. The fitting procedure for a set of images at an epoch involves an interplay between the centroids, the ePSF, and the transformation between the coordinate system of an image and the fiducial image. An improvement in the centroids leads to more accurate transformations and a better estimate of the ePSF and this is iterated until a stable solution ensues. Averaging the centroids from each image transformed to the coordinate system of the fiducial image produces the coordinate for an object at one epoch and its

uncertainty. The fiducial coordinate systems for different epochs are generally offset from each other because of small changes in the telescope pointing and rotation and are also not congruent because of changes in image scale and telescope motion (the aberration of starlight).

4. Determine the motion of the QSO in a "standard" coordinate system. In this coordinate system, the stars of the dSph are at rest while all other objects move. A proper motion of the dSph derives from the reflex motion of the QSO in this coordinate system. The standard coordinate system is defined as the fiducial coordinate system of the first epoch. The $X$ and $Y$ coordinates of a star of the dSph in this system are the average of its coordinates at the three epochs transformed into the standard coordinate system. A six-parameter linear transformation converts coordinates to the standard coordinate system. The transformation also includes a fitted linear motion for the QSO and, iteratively, for objects whose large scatter in their transformed coordinates indicate that they are not members of the dSph. For data taken with PC2, an additional term in the transformation that is linear with $y$ and depends on the flux of an object corrects the effects caused by charge traps.

Both STIS and WFPC2 exhibit geometric distortions which are several pixels at the edge of the field. These are large compared to the approximately 0.001 pixel precision in measuring the positions of objects required to determine the proper motion of a dSph. Even the accuracy with which the distortions are known is larger than the required precision, so our observations must minimize the impact of the distortions. Thus, the observations attempted to place objects on the same pixels of the CCD at each epoch. If the execution of this plan were perfect, no correction for the distortions would have been necessary. Although the roll angles are similar to a high degree, there are linear offsets between epochs on the order of a few tens of pixels. Therefore, our method corrects the distortions using the prescriptions from the STIS Data Handbook (Brown et al. 2002) for the data taken with STIS and from Anderson & King (2003) for the data taken with WFPC2.

An error in the manufacture of the WFPC2 CCDs makes every 34th row in the PC2 images narrower than the other rows (Shaklan et al. 1995). Dubbed the "34th-row defect," it can produce a spurious contribution to the measurement of the proper motion. Our method corrects the centroids for the effect of this defect using the prescription from Anderson & King (1999).

### 4.1. Flux Residuals

Piatek et al. (2002) developed diagnostics for the performance of their algorithm that determines the centroids of objects. The remainder of this section describes the "flux residual" and "position residual" diagnostics and how the algorithm performed in the three fields.

The flux residual diagnostic, $\mathcal{RF}$, defined by Equation 22 in Piatek et al. (2002) is a measure of how well the constructed ePSF matches an image of an object. If the match is perfect, $\mathcal{RF} = 0$. However, if the image of an object is wider than the ePSF, $\mathcal{RF} > 0$; otherwise, $\mathcal{RF} < 0$. If $\mathcal{RF}$ does depart from zero, the departure increases with increasing S/N for an object.

Plotting $\mathcal{RF}$ as a function of position in a CCD can reveal potential flaws in the data and analysis. In the presence of only random noise, a plot of $\mathcal{RF}$ *versus* $X$ or $Y$ would show that the points scatter around $\mathcal{RF} = 0$. Any other distribution is undesirable and can mean, for example, that the true PSF varies with position in a CCD, that the constructed ePSF has an incorrect shape, or that the PSF of an object is distinctly different from the ePSF, as it would be in the case of a galaxy with a resolved core.

#### *4.1.1. Flux Residual Diagnostic for the FOR J0240 − 3434 Field*

Figure 6 plots $\mathcal{RF}$ *versus* $X$ in the left column and $\mathcal{RF}$ *versus* $Y$ in the right column for the FOR J0240−3434 field imaged with PC2. From top to bottom, the plots are for the epochs 1999, 2001, and 2003. Solid squares mark the points corresponding to image A of the QSO, whereas the solid triangles do the same for image B. All of the plots show a modest "bow-shaped" dependence of $\mathcal{RF}$ on $X$ and $Y$ indicating that the true PSF varies with location. The constructed ePSF is narrower than the true PSF around the edges of the CCD and wider near the center. The values of $\mathcal{RF}$ for both images of the QSO tend to be negative; those for image A are more negative than those for image B, most likely because of the variation of the PSF across the image. The $\mathcal{RF}$ for the QSO is more negative than those of most nearby stars, which could be due to the higher S/N of the QSO or, perhaps, to a narrower PSF caused by the bluer color of the QSO.

#### *4.1.2. Flux Residual Diagnostic for the FOR J0240 − 3438 Field*

Figure 7 plots $\mathcal{RF}$ *versus* $X$ (left column) and $\mathcal{RF}$ *versus* $Y$ (right column) for the FOR J0240 − 3438 field imaged with STIS. From top to bottom, the rows of plots are for the epochs 2000, 2001, and 2002. The values of $\mathcal{RF}$ for the QSO are positive for all epochs and most of these points are outside of the top boundary in the upper two rows of plots. The PSF of the QSO is thus wider than the ePSF, most likely because, with a redshift of 0.38, this QSO is near enough for its core to be resolved.

The values of $\mathcal{RF}$ for stars in the top and bottom rows of plots are well behaved. They show no clear trends with either $X$ or $Y$ and scatter around $\mathcal{RF} = 0$. A few bright stars have $\mathcal{RF}$s comparable to those for the QSO. However, the plots in the middle row are not well behaved. The plot of $\mathcal{RF}$ *versus* $X$ shows a clear trend: $\mathcal{RF}$s tend to be positive for $X \lesssim 500$ pixel and negative otherwise. A line with negative slope crossing $\mathcal{RF} = 0$ around $X \approx 500$ pixel could fit the trend. Although the plot of $\mathcal{RF}$ *versus* $Y$ does not show trends, the scatter around $\mathcal{RF} = 0$ is larger than that in the corresponding plots at the other two epochs. The likely cause for this behavior is a dependence of the PSF with $X$. Remembering that the ePSF is a global average of individual PSFs, the PSF is wider than average for $X \lesssim 500$ pixel and narrower than average for greater values of $X$. A variation of the PSF with $X$ in STIS seems isolated to this field and epoch. We are unable to trace the source of this dependence. Position residual diagnostics, $\mathcal{RX}$ and $\mathcal{RY}$, discussed in Section 4.2, will show if the variable PSF had a significant impact on the measured centroids.

#### *4.1.3. Flux Residual Diagnostic for the FOR J0238 − 3443 Field*

Figure 8 for the FOR J0238 − 3443 field is analogous to Figure 7. From top to bottom, the rows of plots are for the epochs 2000, 2001, and 2003.

None of the plots shows a trend between $\mathcal{RF}$ and either $X$ or $Y$. The values of $\mathcal{RF}$ for the QSO tend to be negative — most distinctly in the bottom row of plots — indicating that the PSF of the QSO is narrower than the ePSF.

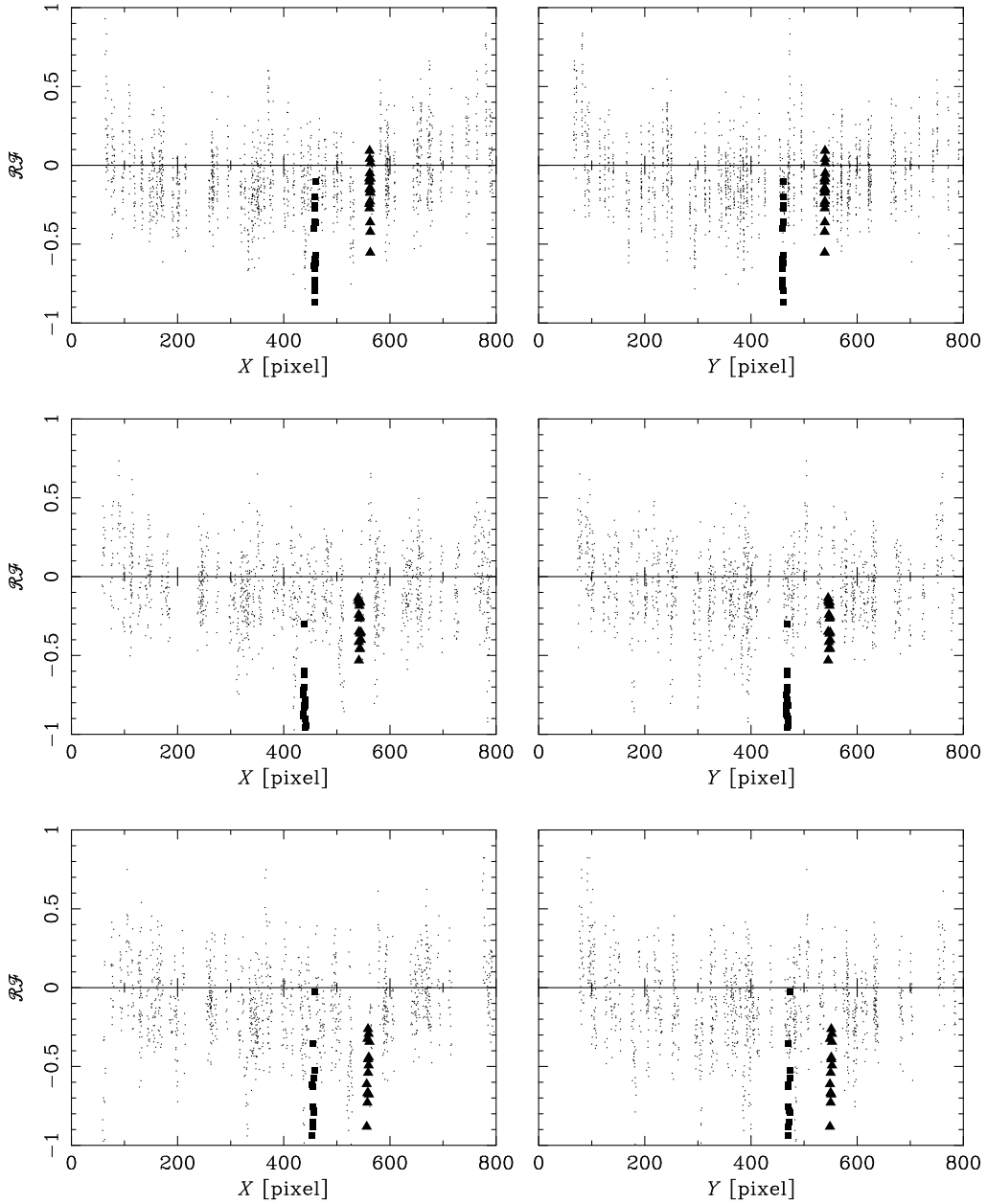


Fig. 6.— Left column: Flux residual $\mathcal{RF}$ as a function of $X$. Right column: Flux residual $\mathcal{RF}$ as a function of $Y$. The plots are for the FOR J0240 − 3434 field that was imaged with PC2. From top to bottom, the rows of plots are for 18 images at epoch 1999, 16 at 2001, and 16 at 2003, respectively. The figure shows points only for those objects that have S/N > 15. The solid squares mark points corresponding to image A of the QSO, while the solid triangles do the same for image B.

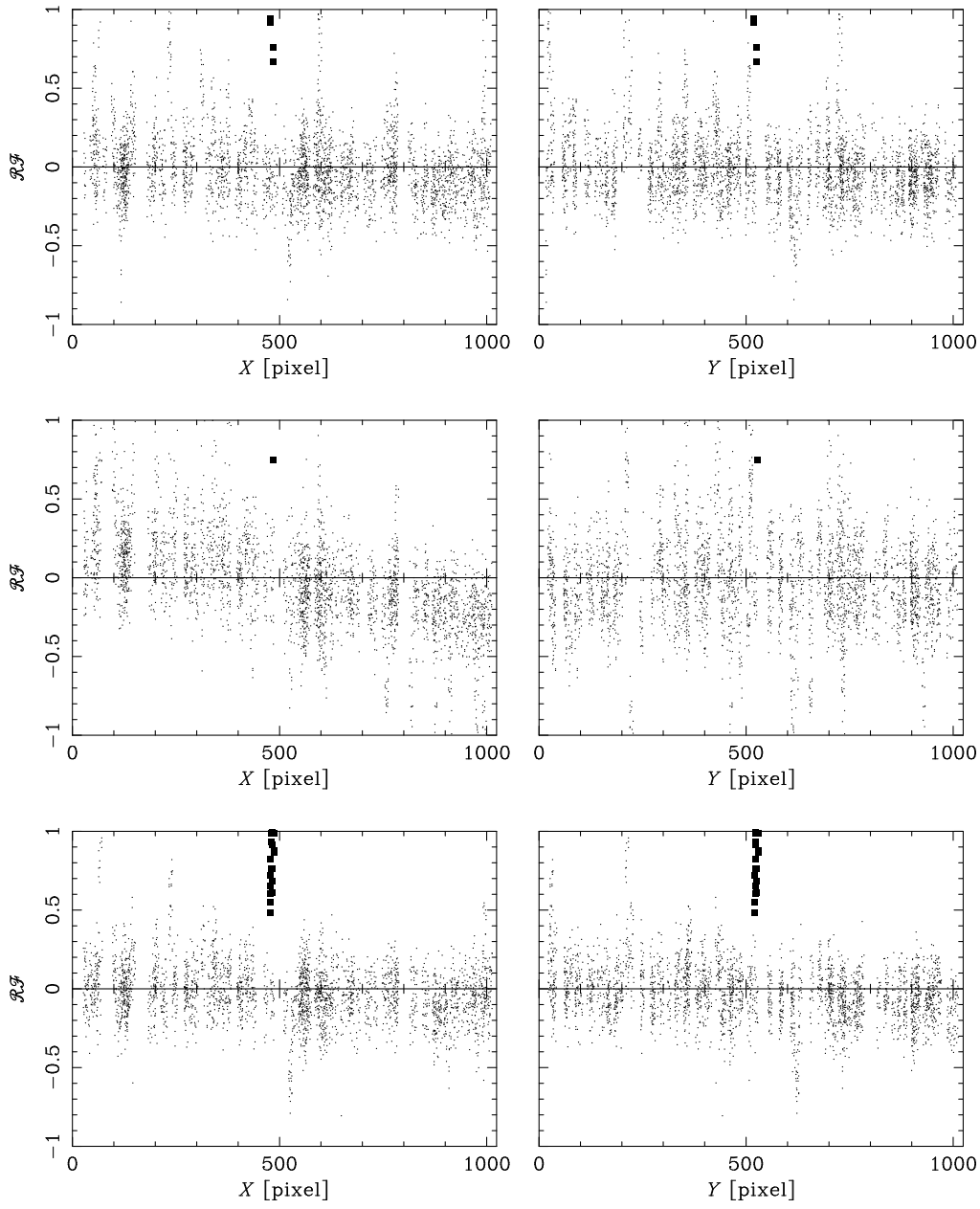


Fig. 7.— Left column: Flux residual $\mathcal{RF}$ as a function of $X$. Right column: Flux residual $\mathcal{RF}$ as a function of $Y$. The plots are for the FOR J0240 − 3438 field, which was imaged with STIS. From top to bottom, the rows of plots are for 24 images at each of epoch 2000, 2001, and 2002, respectively. The figure shows points only for those objects that have $S/N > 15$. The solid squares mark points corresponding to the QSO.

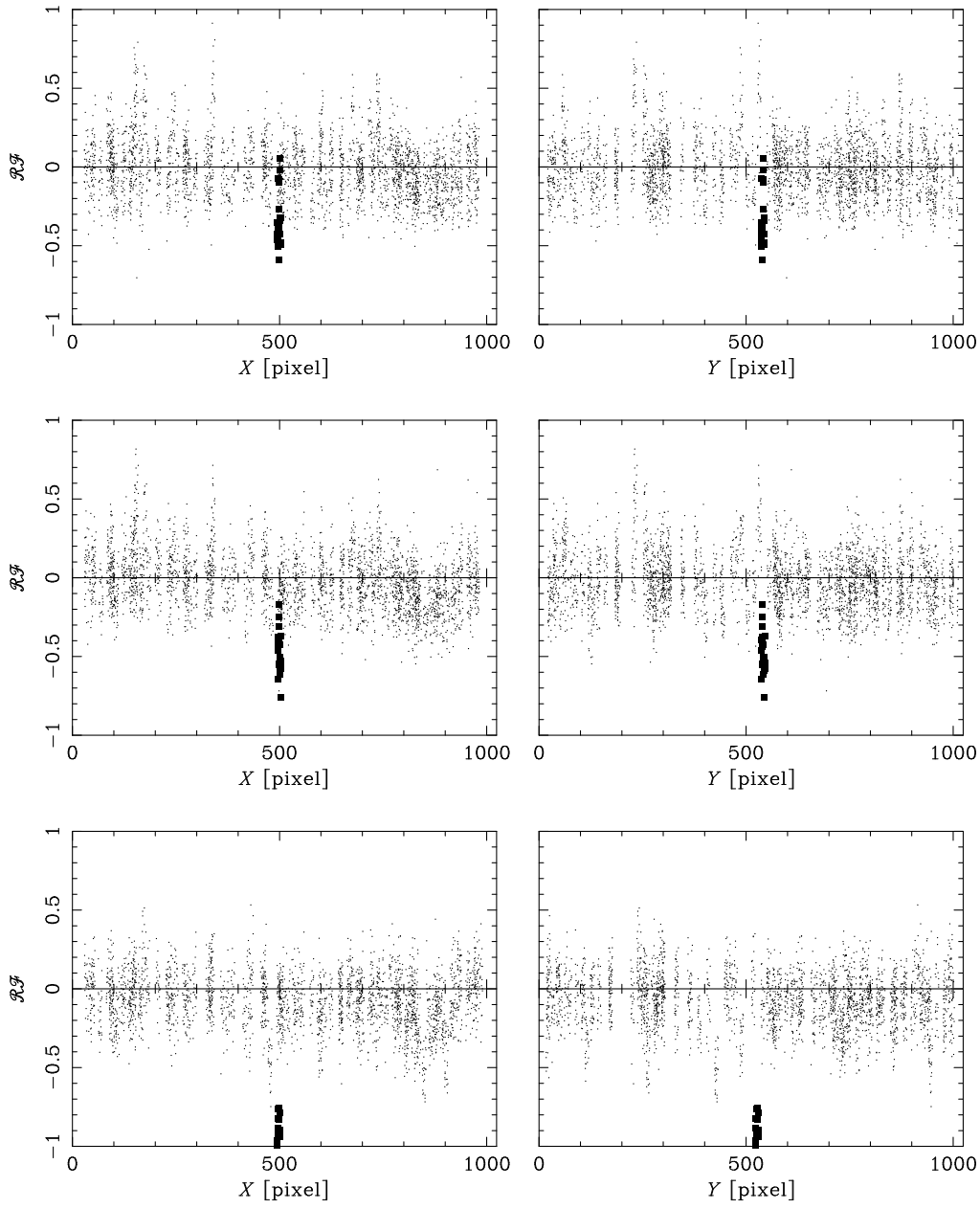


Fig. 8.— Left column: Flux residual $\mathcal{RF}$ as a function of $X$. Right column: Flux residual $\mathcal{RF}$ as a function of $Y$. The plots are for the FOR J0238 − 3443 field, which was imaged with STIS. From top to bottom, the rows of plots are for 24 images at each of the epochs 2000, 2001, and 2003, respectively. The figure shows points only for those objects that have S/N > 15. The solid squares mark points corresponding to the QSO.

### 4.2. Position Residuals

The position residual diagnostic consists of plots of the position residuals $\mathcal{RX} \equiv \langle X_0 \rangle - X_0$ and $\mathcal{RY} \equiv \langle Y_0 \rangle - Y_0$ *versus* the pixel phase $\Phi_x \equiv X_0 - \mathrm{Int}(X_0)$ and $\Phi_y \equiv Y_0 - \mathrm{Int}(Y_0)$. Here $\langle X_0 \rangle$ and $\langle Y_0 \rangle$ are the components of the mean centroid in the fiducial coordinate system — the system of the first image in time at a given epoch. The function $\mathrm{Int}(x)$ returns the integer part of a variable $x$. The coordinate transformation to a fiducial system involves translation, rotation, and scale change. The coefficients of the transformation result from a least-squares fit using objects common to the fiducial image and the one transformed to it.

In the presence of only random errors, position residuals would scatter around $\mathcal{RX} = 0$ or $\mathcal{RY} = 0$ with constant $rms$ for all values of $\Phi_x$ or $\Phi_y$. Trends and structures in the plots are symptomatic of systematic errors.

#### *4.2.1. Position Residual Diagnostic for the FOR J0240 − 3434 Field*

Figure 9 shows plots of the position residuals *versus* pixel phase for the FOR J0240 − 3434 field. Panels *a*, *b*, and *c* are for epochs 1999, 2001, and 2002, respectively. Only two plots, $\mathcal{RX}$ *versus* $\Phi_x$ and $\mathcal{RY}$ *versus* $\Phi_y$, in Figure 9*a* show evidence for trends among the points for images A and B of the QSO. In the first of these two plots, the values of $\mathcal{RX}$ are mostly positive up to $\Phi_x \approx 0.8$ and then negative for larger values of $\Phi_x$. In the second, the $\mathcal{RY}$s show a sinusoidal dependence on $\Phi_y$.

No plot for any epoch shows trends or structures for points corresponding to stars, though we caution that the small number of points and their large scatter due to the modest S/N of the majority of stars would make such trends and structures hard to see.

Even though Figure 6 implies that the PSF varies with position in the image at all three epochs for this field, Figure 9 shows that the QSO has pixel phase errors only at the first epoch. Thus, the origin of the pixel phase errors for the QSO are not clearly caused by the variation of the PSF with position in the field. Neither are they clearly caused by the variation of the PSF between images at one epoch because, as Figure 6 shows, that variation is similar at all three epochs.

#### *4.2.2. Position Residual Diagnostic for the FOR J0240 − 3438 Field*

Figure 10 plots $\mathcal{RX}$ and $\mathcal{RY}$ *versus* $\Phi_x$ and $\Phi_y$ for the FOR J0240 − 3438 field. Panels *a*, *b*, and *c* are for epochs 2000, 2001, and 2002, respectively.

None of the plots in Figure 10*a* shows convincing evidence for systematic errors. However, the plots of $\mathcal{RX}$ *versus* $\Phi_x$ in Figures 10*b* and 10*c* do. In the first plot, $\mathcal{RX}$ has a linear trend with $\Phi_x$ with positive slope. In the second plot, the trend is more sinusoidal. In both plots, $\mathcal{RX}$s corresponding to stars show greater scatter than $\mathcal{RY}$s for the same objects. To a lesser degree, the plot of $\mathcal{RY}$ *versus* $\Phi_y$ in Figure 10*c* shows a sinusoidal trend too.

As is the case for the previous field, there is not a clear correlation between a variation of the PSF with position and the presence of pixel phase errors for the QSO. For the 2001 epoch, both a variation of the PSF with $X$ and pixel phase errors in $X$ are present. In contrast, for the 2002 epoch, pixel phase errors are present even though the PSF does not vary with position. The 2002 epoch has better agreement than the 2000 and 2001 epochs between the PSF of the QSO and that of the stars and it also shows less variation of

Fig. 9a

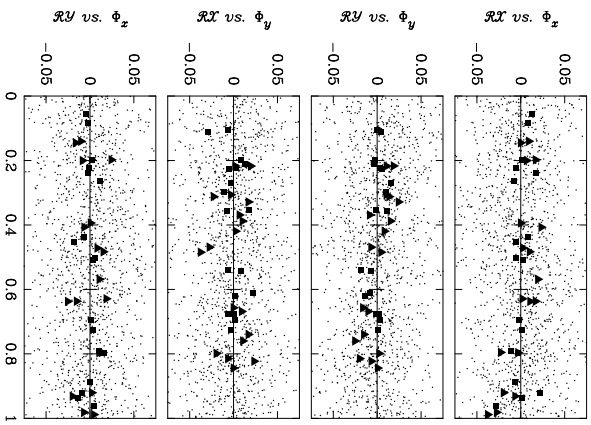


Fig. 9b

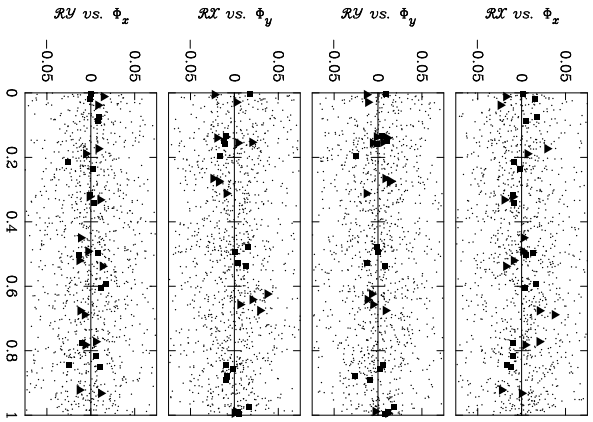


Fig. 9c

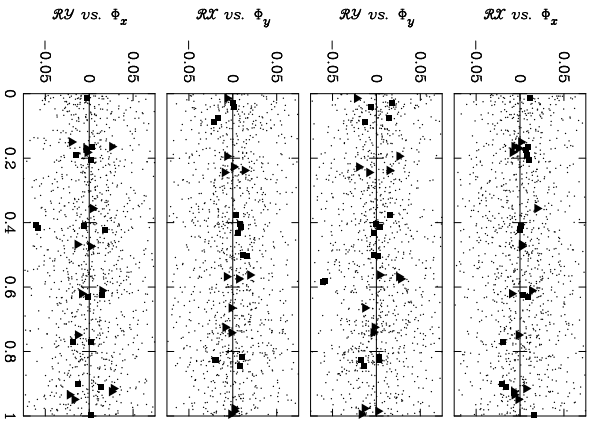


Fig. 9.— Plots for the FOR J0240 − 3434 field of the position residuals, $\mathcal{RX}$ and $\mathcal{RY}$, as a function of the pixel phase, $\Phi_x$ and $\Phi_y$. Panels *a*, *b*, and *c* are for the epochs 1999, 2001, and 2002, respectively. Solid squares and triangles correspond to images A and B of the QSO, respectively. The plots show points only for those objects with S/N > 15.

the PSF between the images of an epoch.

#### *4.2.3. Position Residual Diagnostic for the FOR J0238 − 3443 Field*

Figure 11 plots $\mathcal{RX}$ and $\mathcal{RY}$ *versus* $\Phi_x$ and $\Phi_y$ for the FOR J0240 − 3438 field. Panels *a*, *b*, and *c* are for epochs 2000, 2001, and 2003, respectively.

No plot in the three panels shows clear evidence for systematic errors. The absence of systematic trends in these plots is consistent with the absence of trends in Figure 8.

## 5. The Proper Motion of Fornax

At this point in the analysis, there are three lists of coordinates — one per epoch — for each field. Equations (1) - (4) in Piatek et al. (2006) give the form of the transformation between epochs. This most-general linear transformation has six free parameters $c_1 - c_6$. The transformation also includes an additional term that is linear with $Y$ (see Equations (7) and (8) in Piatek et al. (2005)) if the fitting procedure corrects for the effects caused by decreasing charge transfer efficiency. The slope of the linear correction, $b$, is an adjustable parameter and this correction is applied only to objects whose S/N is below a specified limit.

The systematic errors in the object coordinates reflected in the trends in $\mathcal{RF}$, $\mathcal{RX}$, and $\mathcal{RY}$ with $X$, $Y$, $\Phi_x$, and $\Phi_y$ will contribute to the error in the centroid of an object transformed to the standard coordinate system. Because we are unable to eliminate the source of these trends, our procedure propagates these errors into the uncertainty in the proper motion by increasing the uncertainties in the coordinates of all objects until the $\chi^2$ of the scatter around the transformation is equal to one per degree of freedom (see the discussions in Piatek et al. (2005) and Piatek et al. (2006)).

### 5.1. Motion of the QSOs in the FOR J0240 − 3434 field

The PC was the imaging detector for this field; therefore, correcting for the effects caused by decreasing charge transfer efficiency requires fitting for the parameter $b$. The coordinates of objects with a S/N $< 30$ are corrected using Equation (8) of Piatek et al. (2005). For objects with a larger S/N, the size of the correction decreases linearly with increasing S/N until a value of 100; beyond this value there is no correction. This field contains a lensed QSO with two images, A and B, and so it provides two measurements of the proper motion.

Of the 233, 209, and 231 objects measured at the three epochs, respectively, 191 are common to all epochs. The greatest difference in the pointing of *HST* is between the 1999 and 2001 epochs, where the difference is about 20.6 pixel in the $X$ direction and about 5.6 pixel in the $Y$. The choice for the individual $\chi^2$ that triggers fitting for uniform linear motion is 15. The multiplicative constant that produces a $\chi^2$ of one per degree of freedom is 1.304. The fitted value of $b$ is $-6.5 \times 10^{-5}$.

Figure 12 plots the position residuals, $RX$ and $RY$, defined by Equations (10) and (11) in Piatek et al. (2005) as a function of position in the standard coordinate system. A residual is the difference between the average centroid in the standard coordinate system and the centroid measured at an epoch, corrected for any fitted motion, transformed into the standard coordinate system. The first digit of the subscripts on $RX$ and

Fig. 10a

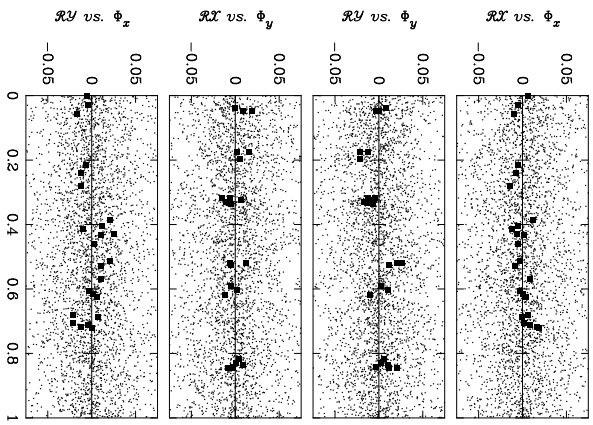


Fig. 10b

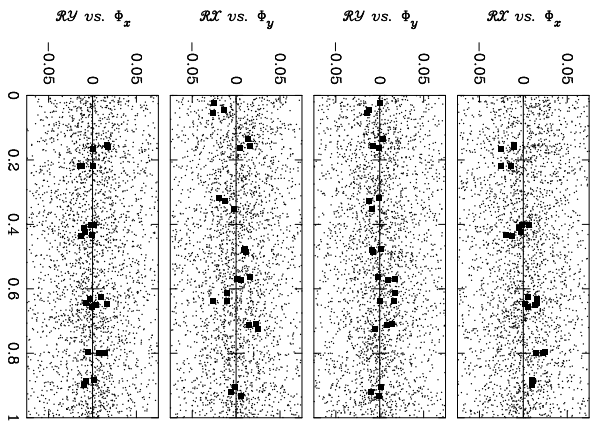


Fig. 10c

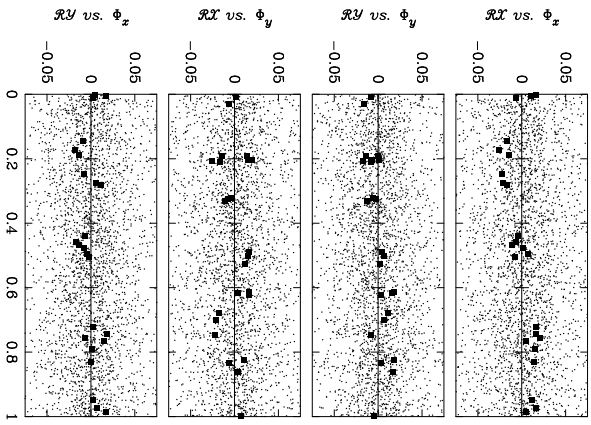


Fig. 10.— Plots for the FOR J0240 − 3438 field of the position residuals, $\mathcal{RX}$ and $\mathcal{RY}$, as a function of the pixel phase, $\Phi_x$ and $\Phi_y$. The panels *a*, *b*, and *c* are for the epochs 2000, 2001, and 2002, respectively. The solid squares mark points for the QSO. The plots show points only for those objects with S/N > 15.

Fig. 11a

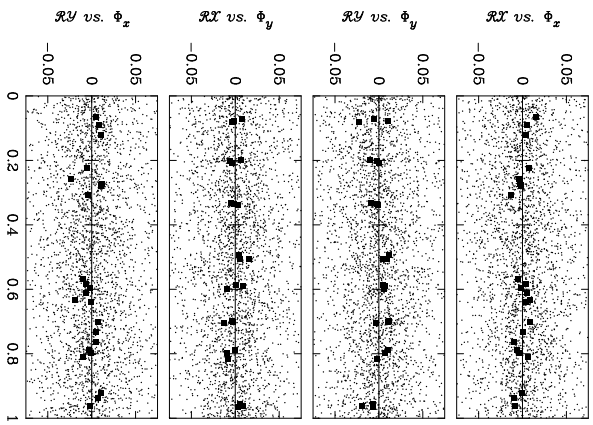


Fig. 11a

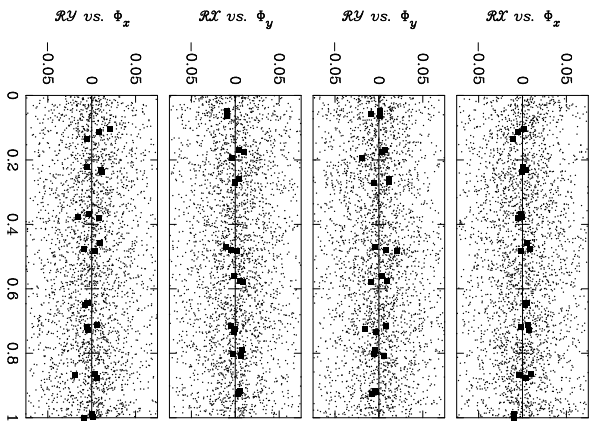


Fig. 11a

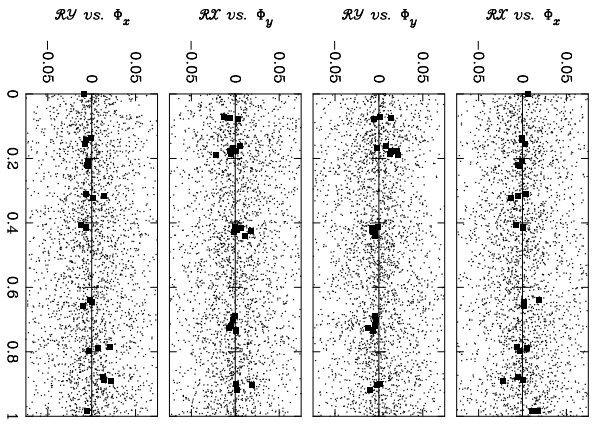


Fig. 11.— Plots for the FOR J0238 − 3443 field of the position residuals, $\mathcal{RX}$ and $\mathcal{RY}$, as a function of the pixel phase, $\Phi_x$ and $\Phi_y$. The panels *a*, *b*, and *c* are for the epochs 2000, 2001, and 2003, respectively. The solid squares mark points for the QSO. The plots show points only for those objects with S/N > 15.

$RY$ in the figure indicates the epoch of the measurement. None of the plots shows a trend between $RX$ and $X$ or $RY$ and $Y$. Although this article does not show them, the plots of $RX$ versus $Y$ and $RY$ versus $X$ also do not show any trends. Figure 13 plots weighted mean residuals, $\langle RX \rangle$ and $\langle RY \rangle$, in 10 equal-length bins in $X$ or $Y$. The error bar on a point is the usual uncertainty in the weighted mean. The values of $\langle RX \rangle$ and $\langle RY \rangle$ do not show systematic trends for $X$ and $Y$ greater than approximately 150 pixel. However, the two points with $X < 150$ pixel or $Y < 150$ pixel show a combination of large error bars due to a small number of points contributing to the mean and a deviation from $\langle RX \rangle = 0$ pixel or $\langle RY \rangle = 0$ pixel due to a mismatch between the ePSF and PSF near the edges of the chip. The points with the largest $X$ or $Y$ also tend to show a greater than expected deviation, due to the mismatch. The position residuals do not show any systematic trends with respect to S/N, as depicted by Figure 14. The plotted values of the S/N are from the first-epoch data. As expected, the scatter in the values of $RX$ and $RY$ increases with decreasing S/N.

In the standard coordinate system, in which the stars of Fornax are at rest, the QSO moves. Figure 15 depicts such motion for image A. The implied motion from the best-fitting straight lines is $(\mu_x, \mu_y) = (-0.0084 \pm 0.0019, -0.0102 \pm 0.0014)$ pixel yr$^{-1}$. The contribution to the total $\chi^2$ from the QSO is 1.47 for two degrees of freedom. Figure 16 is analogous to Figure 15 for image B. Here, the implied motion is $(\mu_x, \mu_y) = (-0.0043 \pm 0.0020, -0.0132 \pm 0.0024)$ pixel yr$^{-1}$ and the contribution to the total $\chi^2$ is 1.37 for two degrees of freedom. For ease of comparison, the scales of Figures 15 and 16 are identical.

### 5.2. Motion of the QSO in the FOR J$0240 - 3438$ field

The number of objects with a measured centroid is 442, 407, and 431 in epochs 2000, 2001, and 2002, respectively. Among these, 310 objects are common to the three epochs. The greatest difference in the pointing of *HST* is between the 2000 and 2002 epochs, where the difference is about 2.5 pixel in the $X$ direction and about 5.3 pixel in the $Y$. Because the images used in the analysis were corrected for the effects caused by the decreasing charge transfer efficiency, the transformation to the standard coordinate system did not include a term that would account for such effects. The choice for the individual $\chi^2$ that triggers fitting for uniform linear motion is 15. The multiplicative constant that produces a $\chi^2$ of one per degree of freedom is 1.100.

Figure 17 plots $RX$ and $RY$ as a function of position in the standard coordinate system. Although the plots do not show any egregious trends, some subtle structures can be discerned. The points in the plot of $RX$ *versus* $X$ for the 2001 epoch (middle row) have a greater scatter than those in the corresponding plots for the two other epochs and show a "flare up" around $X \approx 300$ pixel. The points in the plot $RY$ *versus* $Y$ also have a greater scatter, which, in contrast, varies little with $Y$. These observations are more apparent in Figure 18. Only the plot of $\langle RX \rangle$ *versus* $X$ for the middle epoch shows a statistically significant deviation of $\langle RX \rangle$ from 0. Here, $\langle RX \rangle$ for $X$ between 300-400 pixel deviates more than 4 $\sigma$ from 0. Figure 19 shows no systematic trends between the position residuals and S/N.

Figure 20 depicts the motion of the QSO in the standard coordinate system. The implied motion from the best-fitting straight lines is $(\mu_x, \mu_y) = (0.0124 \pm 0.0030, -0.0002 \pm 0.0032)$ pixel yr$^{-1}$. The contribution to the total $\chi^2$ from the QSO is 0.98 for two degrees of freedom.

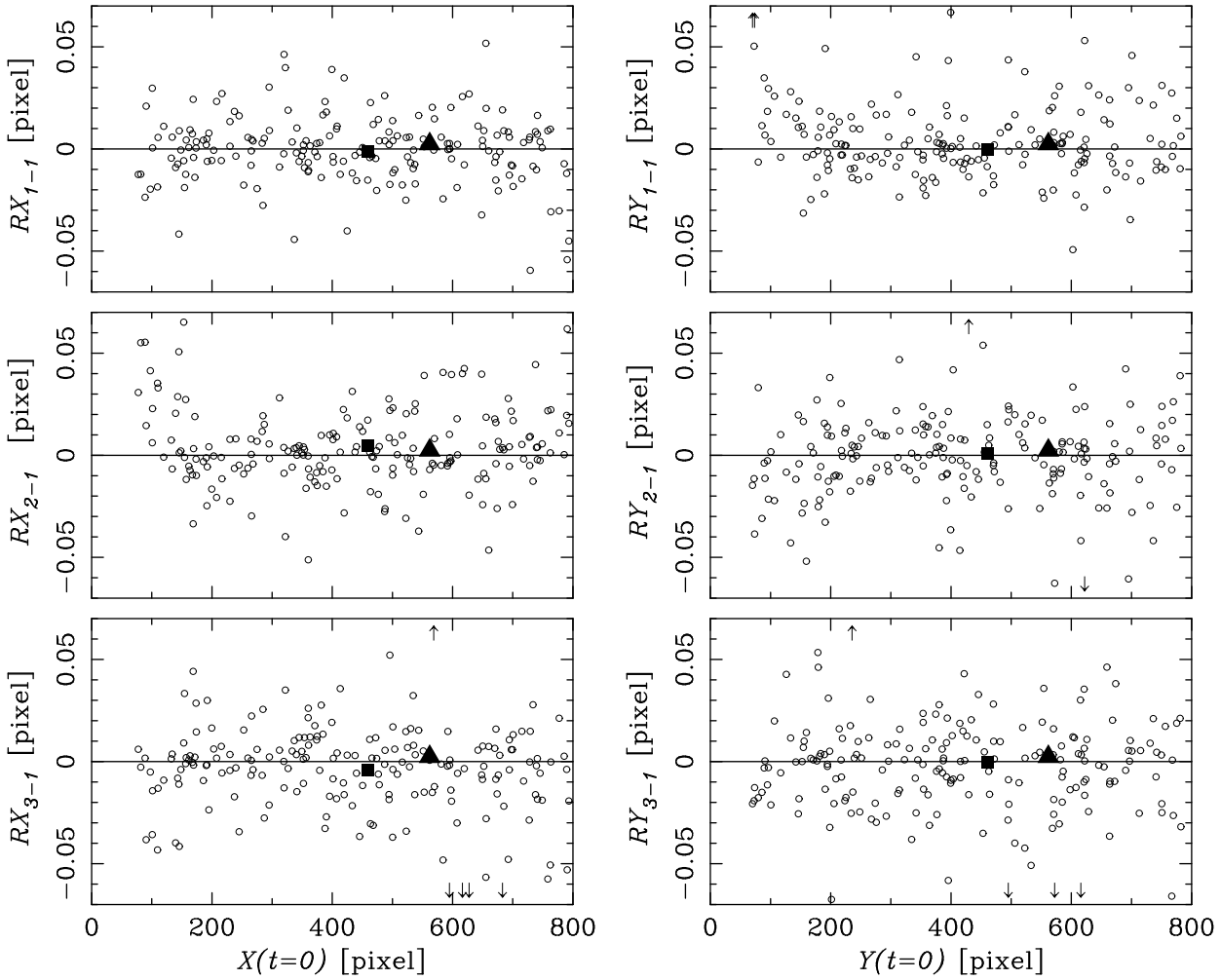


Fig. 12.— Position residuals defined by Equations (10) and (11) in Piatek et al. (2005) for the objects in the FOR J0240 − 3434 field. The epochs increase chronologically from top to bottom. *Left*: $RX$ vs. $X$. *Right*: $RY$ vs. $Y$. The squares correspond to image A of the QSO and the triangles to image B. The arrows indicate points beyond the boundaries of the plot.

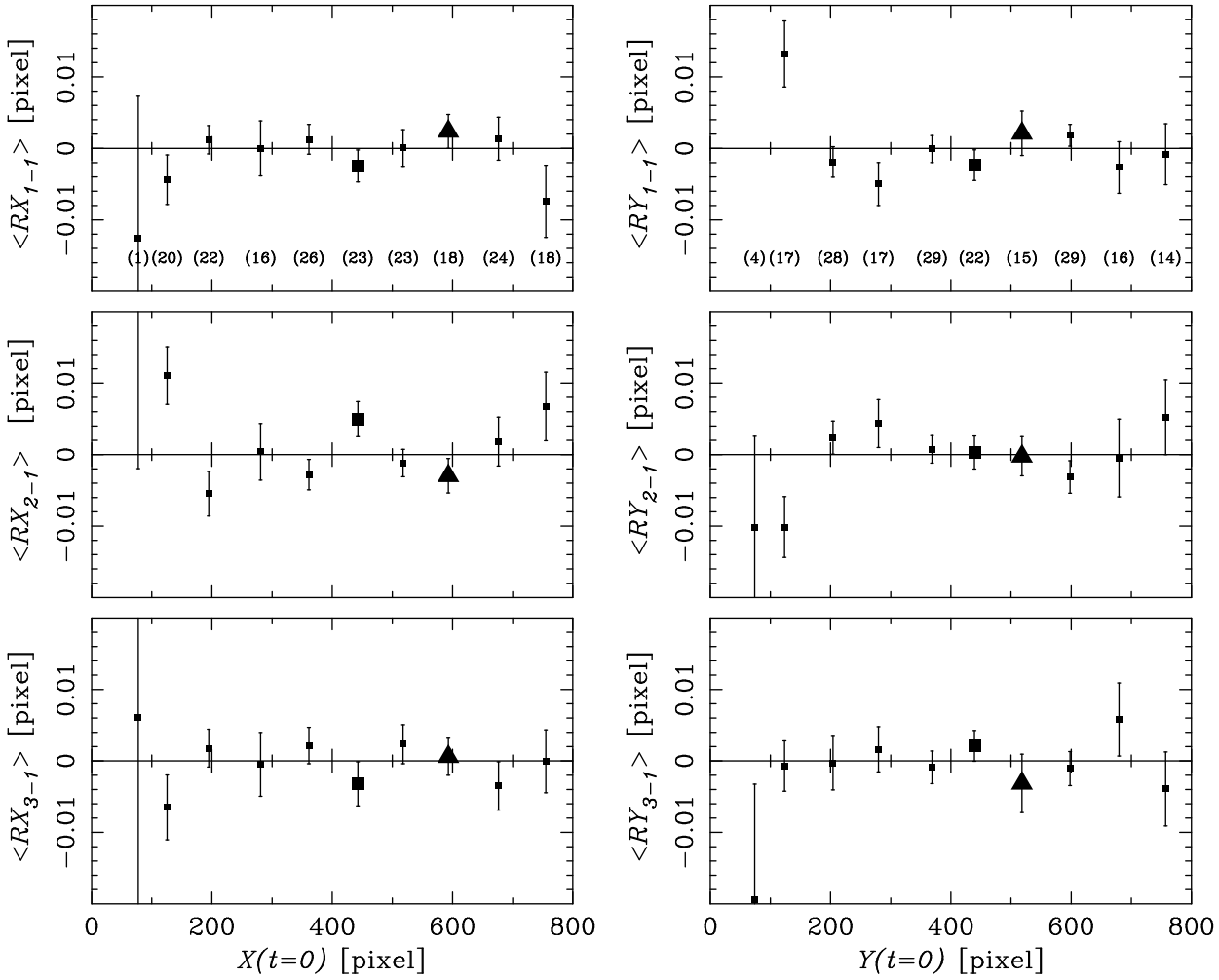


Fig. 13.— Mean position residuals as a function of position for the FOR J0240 − 3434 field. *Left*: $\langle RX \rangle$ vs. $X$. *Right*: $\langle RY \rangle$ vs. $Y$. The points are the weighted mean residuals in 10 equal-length bins in $X$ or $Y$. The points are plotted at the mean of the coordinate values in the bin. The numbers in parenthesis indicate how many values contributed to the mean. The larger squares and triangles mark those points that include contributions to the mean from images A and B of the QSO, respectively.

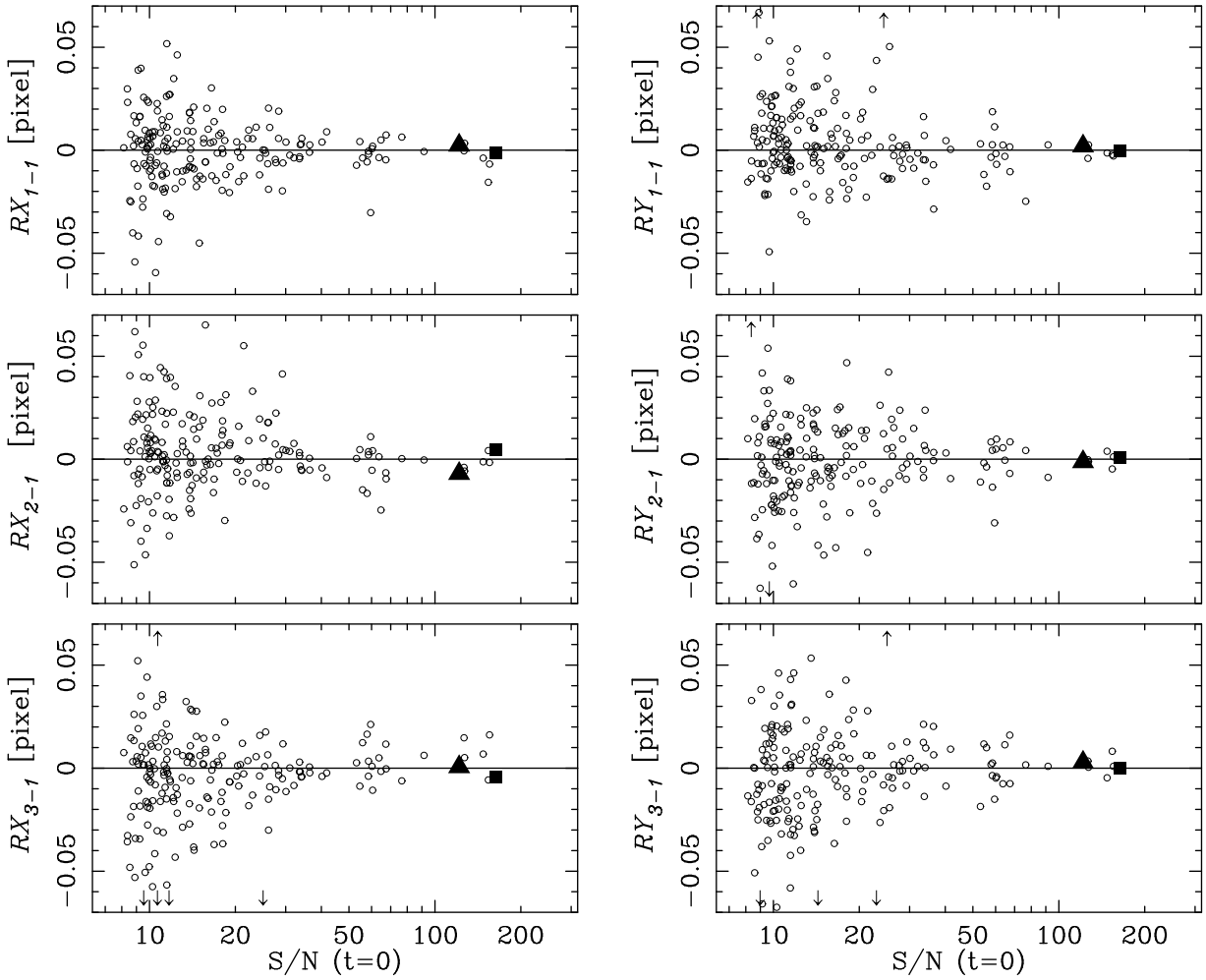


Fig. 14.— Position residuals as a function of S/N for the objects in the FOR J0240 − 3434 field. The epochs increase chronologically from top to bottom. *Left*: *RX* vs. S/N. *Right*: *RY* vs. S/N. The squares correspond to image A of the QSO and the triangles to image B. The arrows indicate points beyond the boundaries of the plot.

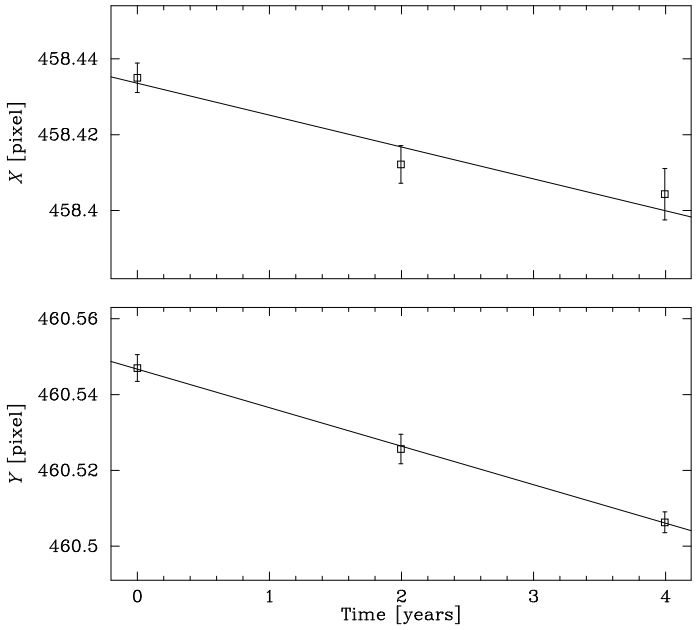


Fig. 15.— Location of image A of the QSO as a function of time for the FOR J0240 − 3434 field in the standard coordinate system.

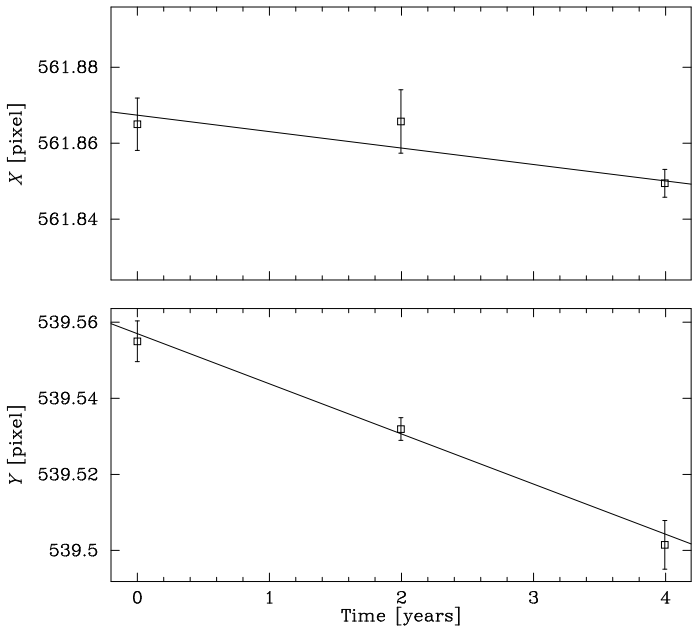


Fig. 16.— Location of the image B of the QSO as a function of time for the FOR J0240 − 3434 field in the standard coordinate system.

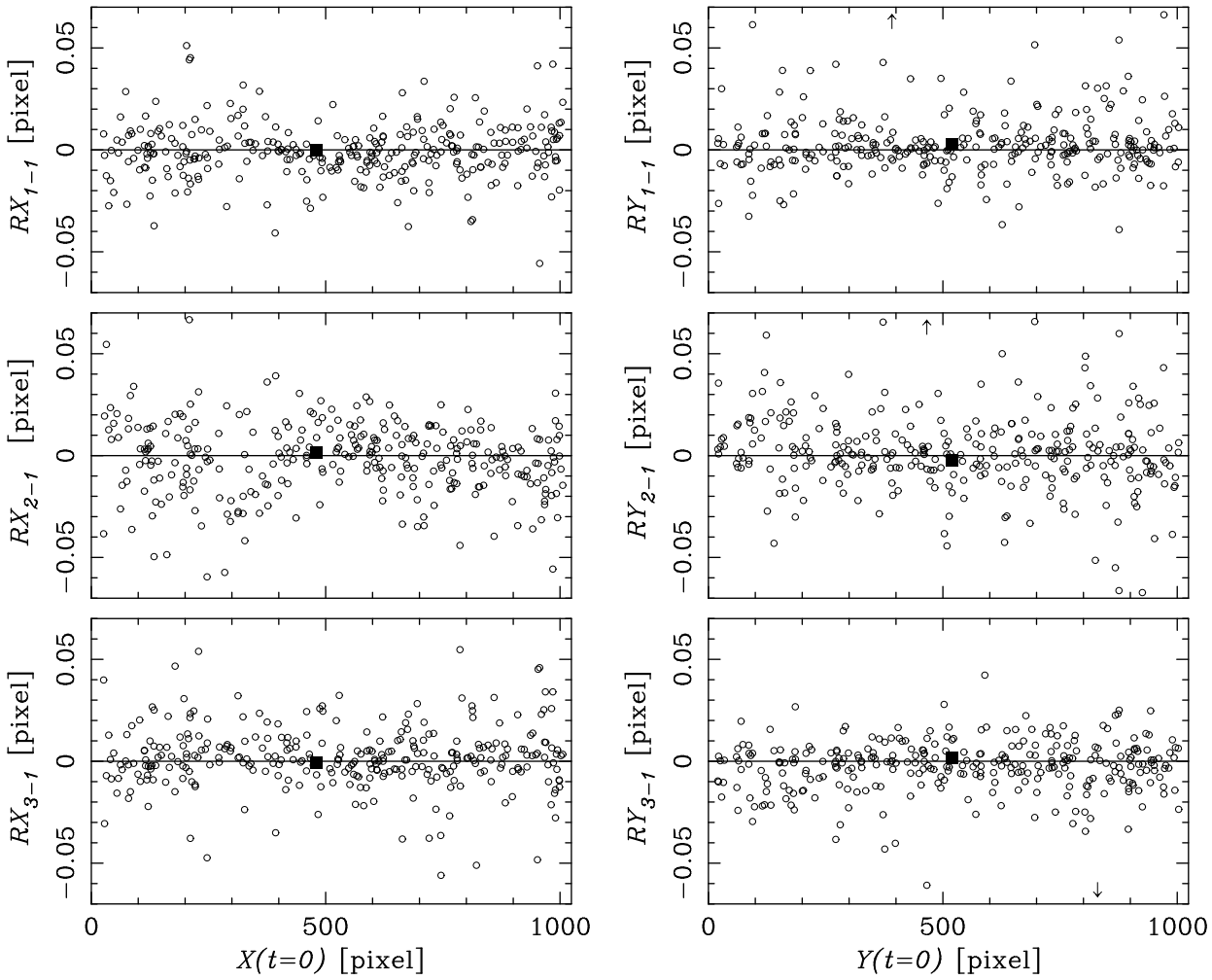


Fig. 17.— Position residuals for the objects in the FOR J0240 − 3438 field. The epochs increase chronologically from top to bottom. *Left*: $RX$ vs. $X$. *Right*: $RY$ vs. $Y$. The squares correspond to the QSO. The arrows indicate points beyond the boundaries of the plot.

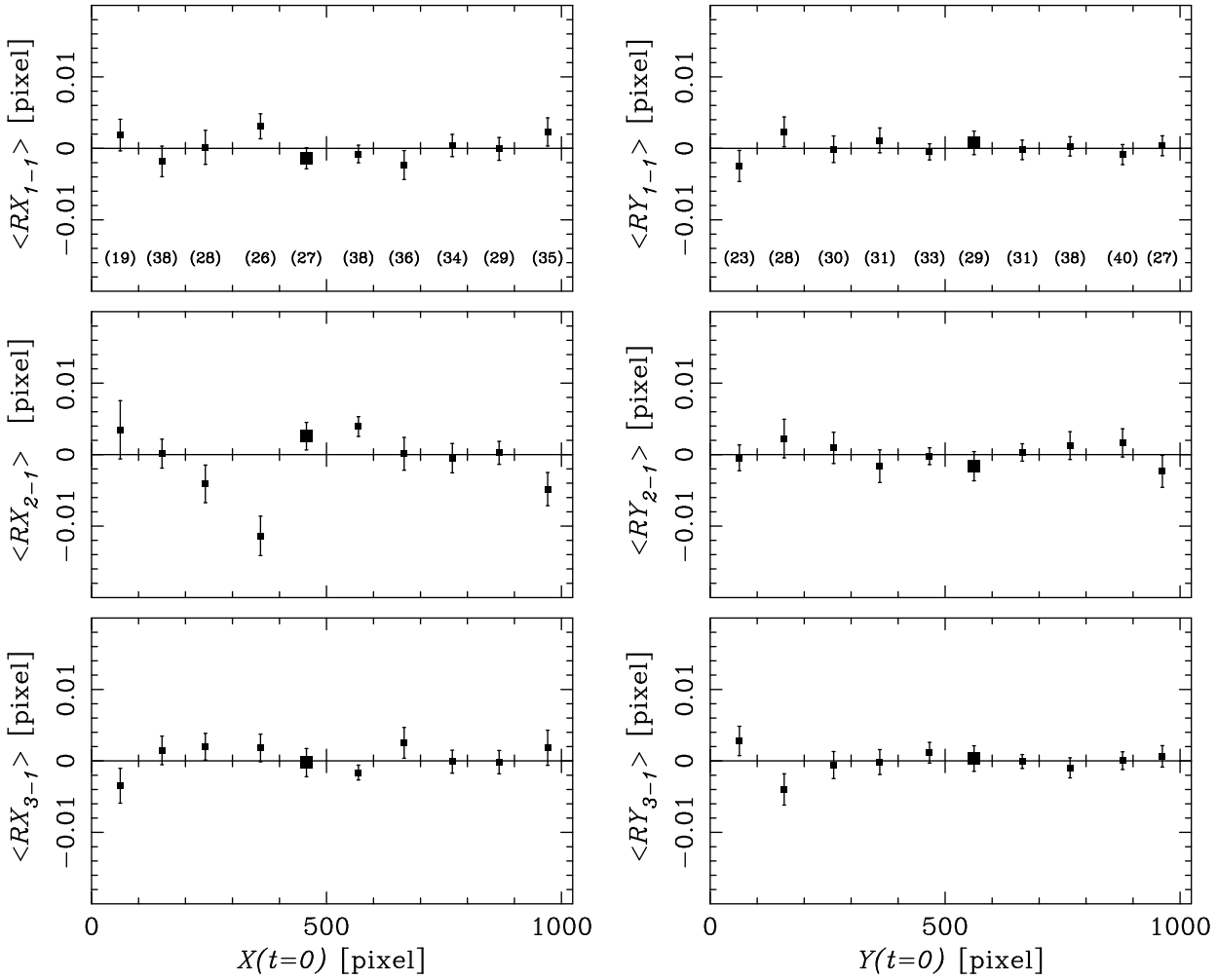


Fig. 18.— Mean position residuals as a function of position for the FOR J0240 − 3438 field. *Left*: $\langle RX \rangle$ vs. $X$. *Right*: $\langle RY \rangle$ vs. $Y$. The points are the weighted mean residuals in 10 equal-length bins in $X$ or $Y$. The points are plotted at the mean of the coordinate values in the bin. The numbers in parenthesis indicate how many values contributed to the mean. The larger squares mark those points that include the contribution to the mean from the QSO.

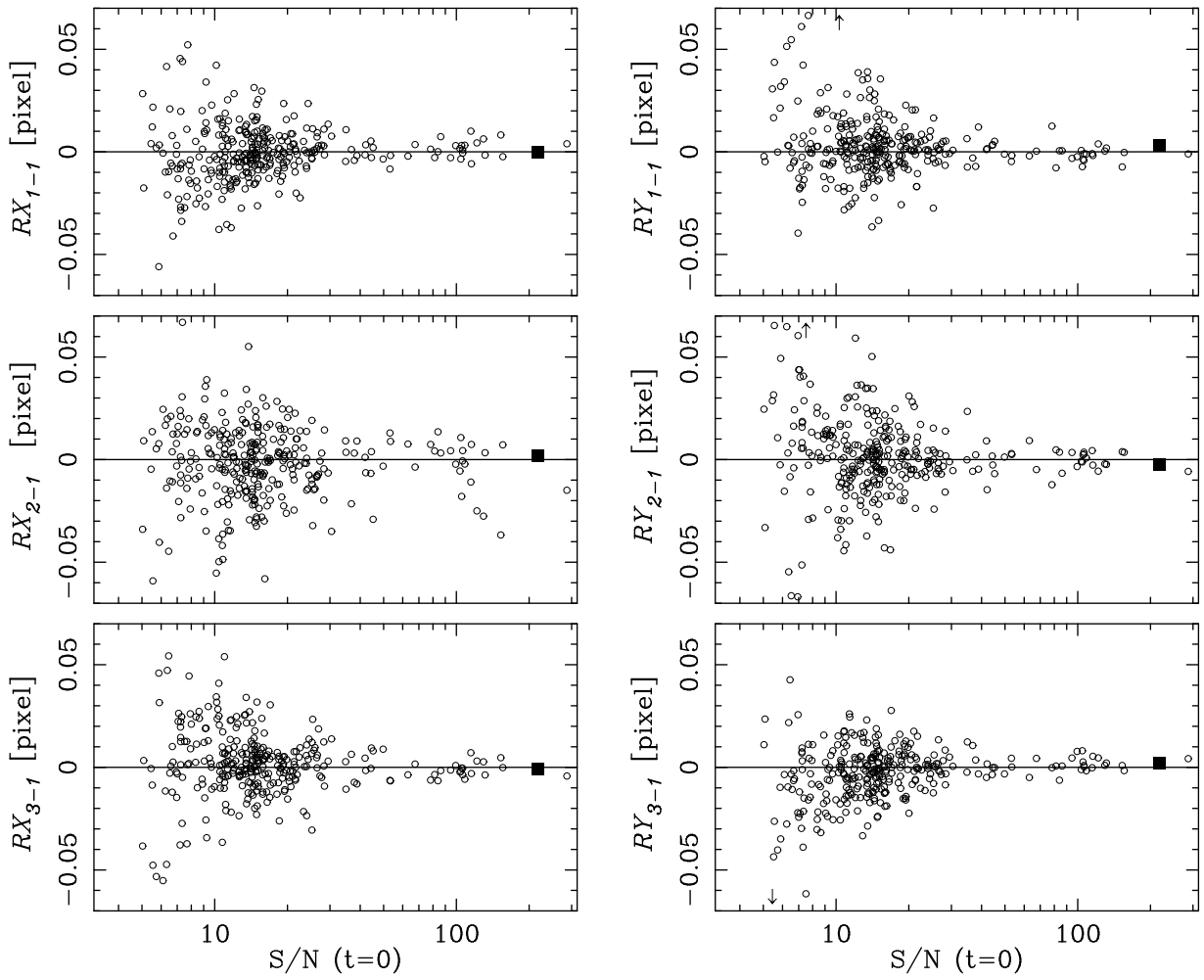


Fig. 19.— Position residuals as a function of S/N for the objects in the FOR J0240 − 3438 field. The epochs increase chronologically from top to bottom. *Left*: *RX* vs. S/N. *Right*: *RY* vs. S/N. The squares correspond to the QSO. The arrows indicate points beyond the boundaries of the plot.

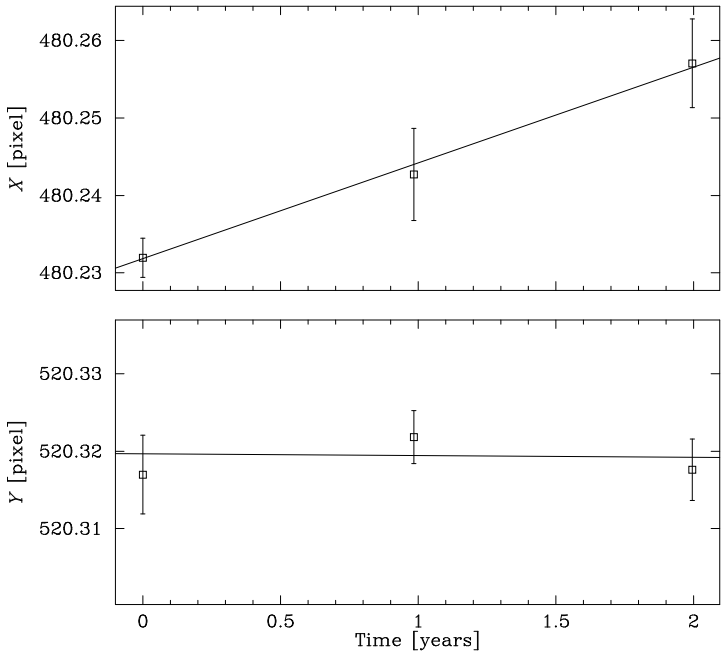


Fig. 20.— Location of the QSO as a function of time for the FOR J0240 − 3438 field in the standard coordinate system. The vertical axis in each plot has the same scale.

### 5.3. Motion of the QSO in the FOR J0238 − 3443 field

The number of objects with a measured centroid is 365, 380, and 347 in epochs 2000, 2001, and 2003, respectively, and 256 are common to all three epochs. The greatest difference in the pointing of *HST* is between the 2001 and 2003 epochs, where the difference is about 2.6 pixel in the $X$ direction and about 15.6 pixel in the $Y$. As for the previous field, the images were corrected for the effects caused by the decreasing charge transfer efficiency. The choice for the individual $\chi^2$ that triggers fitting for uniform linear motion is 15. The multiplicative constant that produces a $\chi^2$ of one per degree of freedom is 1.125.

Figures 21 and 22 for the FOR J0238 − 3443 field are analogous to Figures 17 and 18. The first of these two figures does not show any alarming trends between the residuals and position. The scatter of the points shown in the bottom row of plots — especially in $\langle RX \rangle$ *versus* $X$ — is larger than that in the other plots. The larger error bars and somewhat larger scatter around zero seen in the plot of average residuals confirm this observation. Figure 23, analogous to 19, also does not show any systematic trends between the position residuals and S/N.

Figure 24 shows the motion of the QSO in the standard coordinate system. The implied motion from the best-fitting straight lines is $(\mu_x, \mu_y) = (0.0103 \pm 0.0011, -0.0056 \pm 0.0014)$ pixel yr$^{-1}$. The contribution to the total $\chi^2$ from the QSO is 0.33 for two degrees of freedom.

### 5.4. Measured Proper Motion

Table 3 gives the measured proper motion for each field in the equatorial coordinate system and the weighted mean. Table 4 gives the proper motion for those objects in the FOR J0240 − 3434 field for which

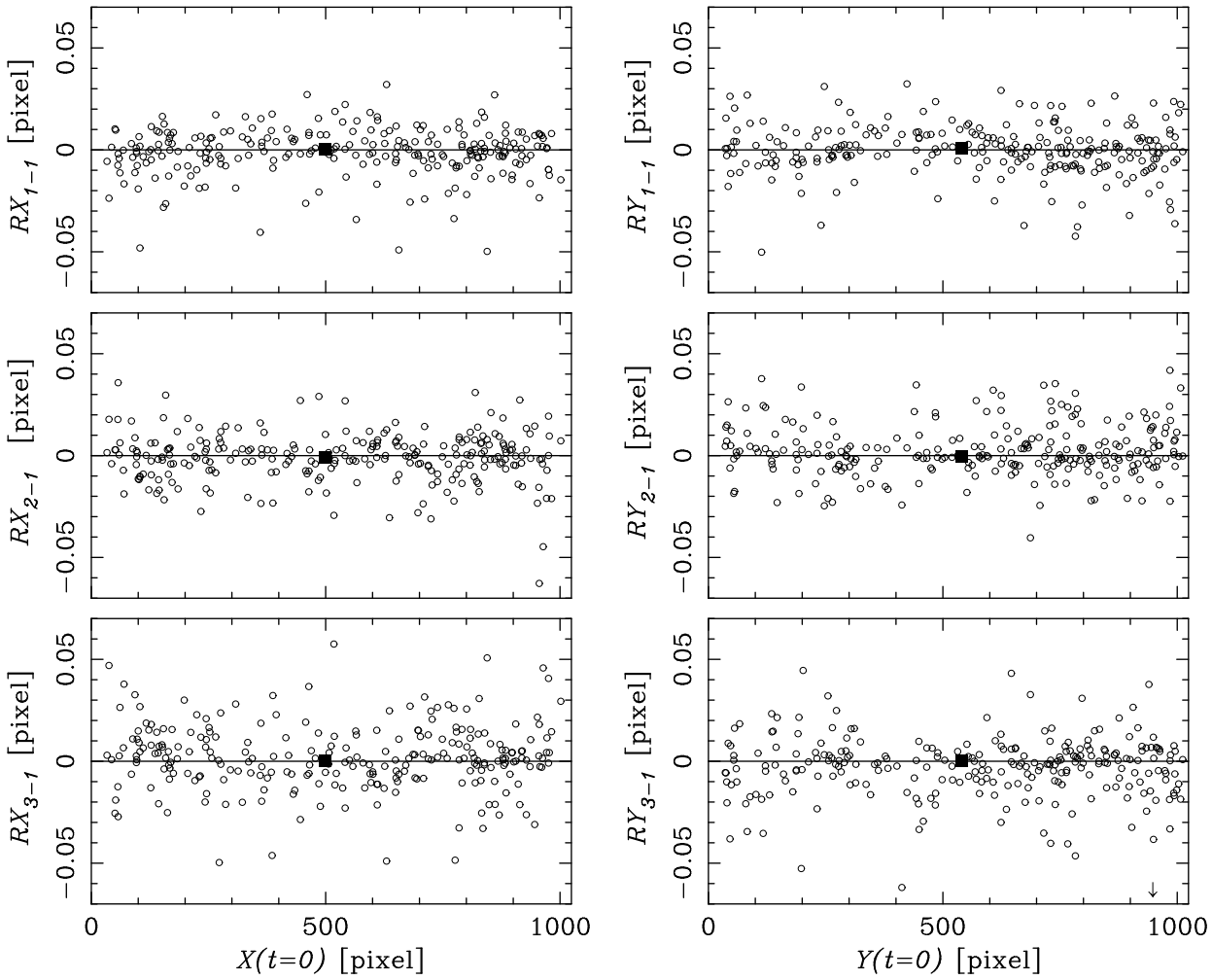


Fig. 21.— Position residuals for the objects in the FOR J0238 − 3443 field. The epochs increase chronologically from top to bottom. *Left*: $RX$ vs. $X$. *Right*: $RY$ vs. $Y$. The squares correspond to the QSO. The arrows indicate points beyond the boundaries of the plot.

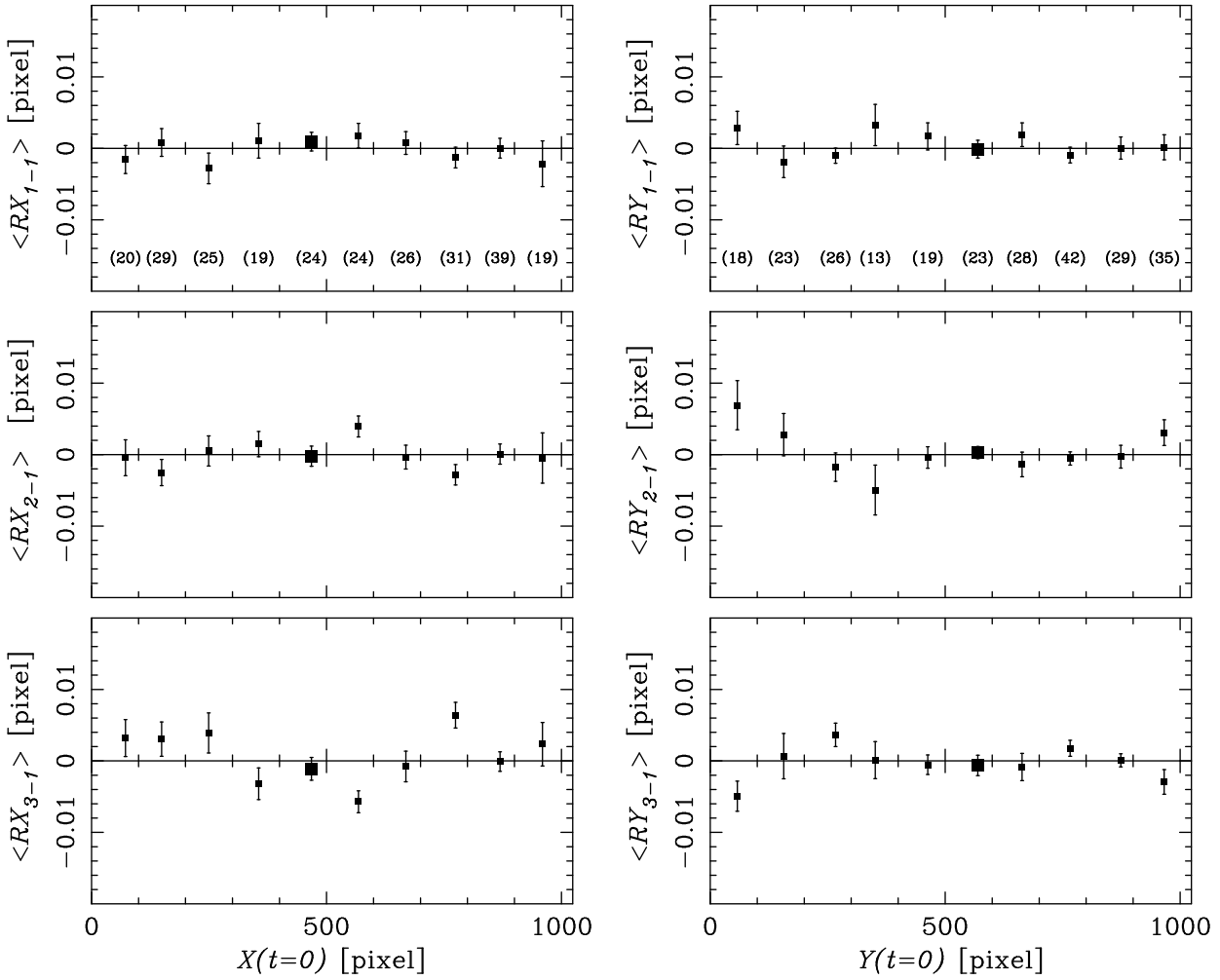


Fig. 22.— Mean position residuals as a function of position for the FOR J0238 − 3443 field. *Left*: $\langle RX \rangle$ vs. $X$. *Right*: $\langle RY \rangle$ vs. $Y$. The points are the weighted mean residuals in 10 equal-length bins in $X$ or $Y$. The points are plotted at the mean of the coordinate values in the bin. The numbers in parenthesis indicate how many values contributed to the mean. The larger squares mark those points that include the contribution to the mean from the QSO.

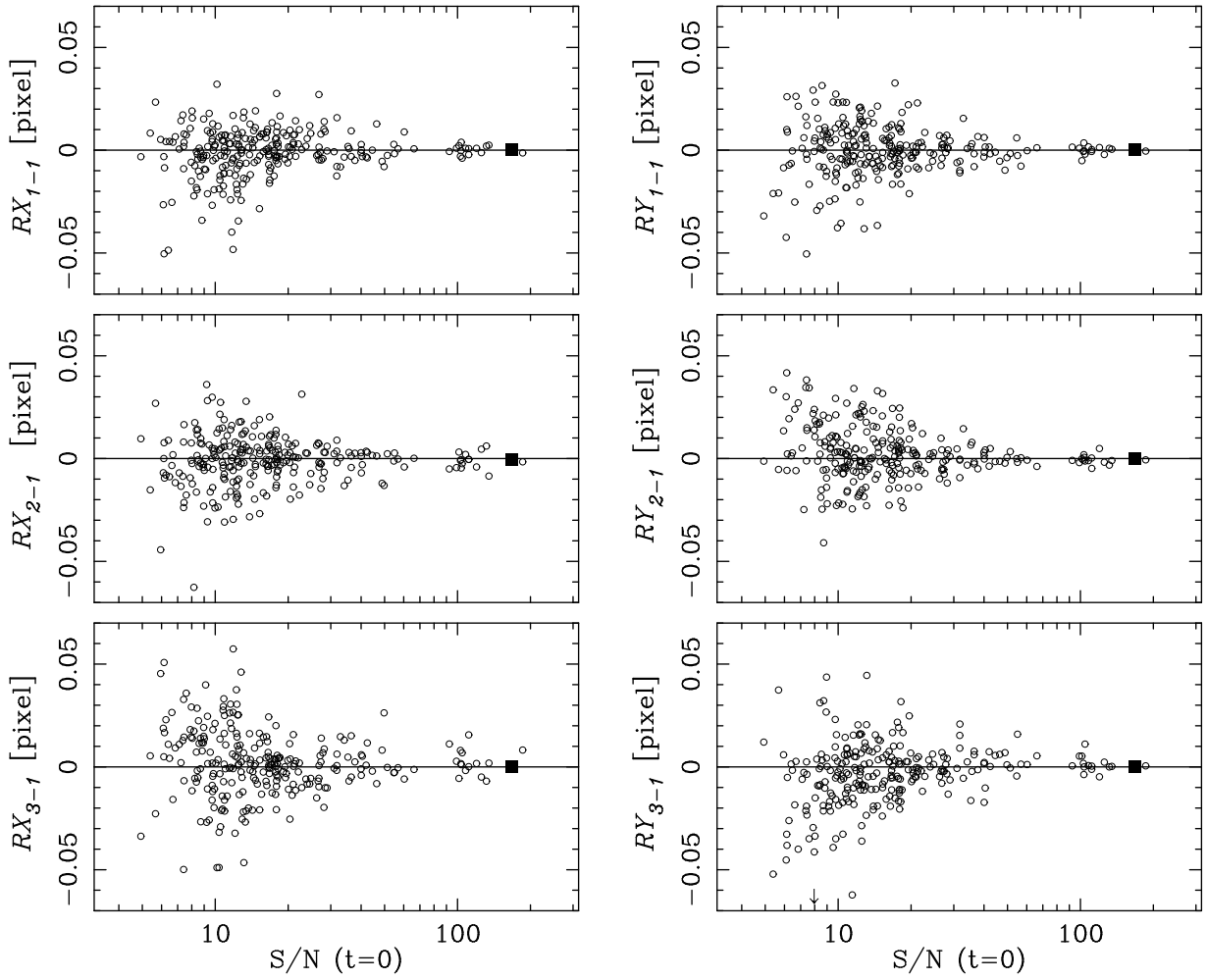


Fig. 23.— Position residuals as a function of S/N for the objects in the FOR J0238 − 3443 field. The epochs increase chronologically from top to bottom. *Left*: *RX* vs. S/N. *Right*: *RY* vs. S/N. The squares correspond to the QSO. The arrows indicate points beyond the boundaries of the plot.

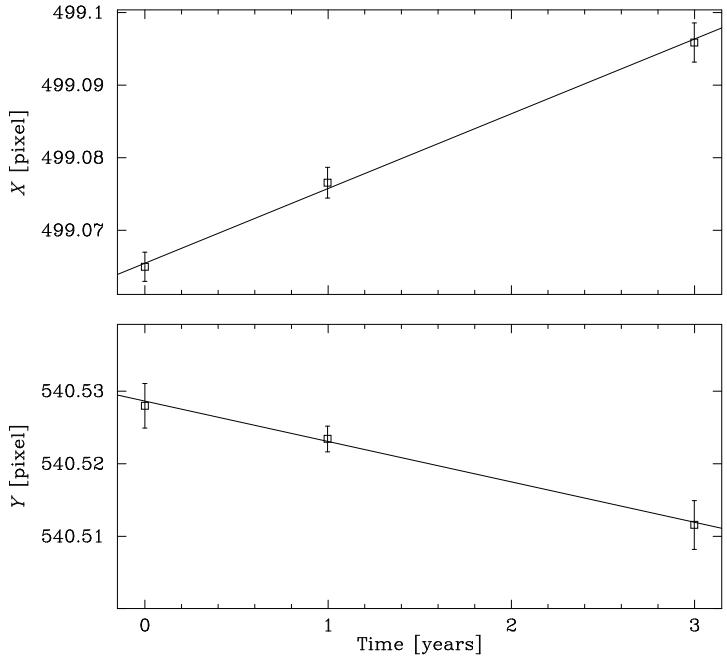


Fig. 24.— Location of the QSO as a function of time for the FOR J0238 − 3443 field in the standard coordinate system. The vertical axis in each plot has the same scale.

it was measured. Tables 5 and 6 do the same for the FOR J0240 − 3438 and FOR J0238 − 3443 fields, respectively. The first two lines in Table 4 and the first lines in Tables 5 and 6 correspond to the QSOs. The subsequent lines list objects in order of decreasing S/N. After column (1) listing the ID of an object, columns (2) and (3) give the $X$- and $Y$-coordinates of the object in the earliest image of the first epoch. These images are u50j0201r, o5bl04010, and o5bl03010 for Tables 4, 5, and 6, respectively. Column (4) gives the average S/N at the first epoch. Columns (5) and (6) give the equatorial components of the measured proper motion. Each value is the sum of the measured motion in the standard coordinate system and the weighted mean proper motion of Fornax given in the bottom line of Table 3. In other words, the listed values are with respect to the QSOs and, thus, the values for the QSOs are listed as 0. The quoted uncertainty is the sum in quadrature of the uncertainty in the motion of an object in the standard coordinate system and the uncertainty of the weighted mean proper motion of Fornax. Column (7) gives the contribution of the object to the total $\chi^2$.

The measured proper motion of Fornax from this article, $(\mu_\alpha, \mu_\delta) = (47.6{\pm}4.6, -36.0{\pm}4.1)$ mas century$^{-1}$, replaces the preliminary measurement in Piatek et al. (2002). Dinescu et al. (2004) reported another independent measurement, $(\mu_\alpha, \mu_\delta) = (59 \pm 16, -15 \pm 16)$ mas century$^{-1}$. For these two independent measurements, the $\alpha$ components differ by 0.68 times the uncertainty of their difference, whereas the $\delta$ components differ by 1.27 times.

Figure 25 compares the measurement from Dinescu et al. (2004) and the four independent measurements from this article. A rectangle represents a single measurement: its center, marked with a circle, is the best estimate of the proper motion and the sides are offset by the 1-$\sigma$ uncertainties. Rectangle 1 represents the measurement from Dinescu et al. (2004), while the other four represent the measurements in this article (see the caption). The $\alpha$ components of all the measurements differ from their mean by less than their

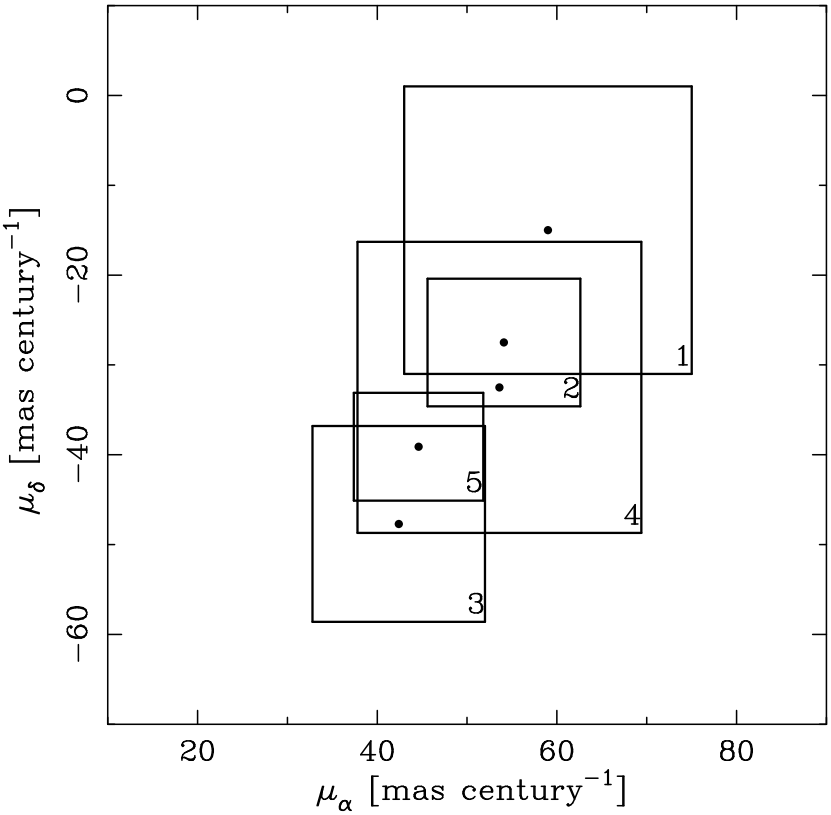


Fig. 25.— Comparison of five independent measurements of the proper motion of Fornax. The center of each rectangle, marked with a circle, is the best estimate of the proper motion, and the sides are offset by the 1 $\sigma$ uncertainties. Rectangles 1 - 5 correspond to the measurements from Dinescu et al. (2004), and from this study for the fields FOR J0240 − 3434A, FOR J0240 − 3434B, FOR J0240 − 3438, and FOR J0238 − 3443, respectively.

uncertainties, whereas the $\delta$ components of some measurements differ by more. For the measurements from this study, the largest difference in the $\delta$ components, for 2 and 3, is 1.55 times its uncertainty. The $\chi^2$ of our measurements around their weighted mean is 1.3 for $\mu_\alpha$ and 2.9 for $\mu_\delta$, each for 3 degrees of freedom. Including the Dinescu et al. (2004) measurement in the weighted mean alters the values by only 1–2 mas century$^{-1}$. The $\chi^2$ of the five measurements around this mean is 1.9 for $\mu_\alpha$ and 4.8 for $\mu_\delta$, each for 4 degrees of freedom. We conclude that the agreement among the five independent measurements is reasonable, implying that the proper motion of Fornax is reliably known.

The result in Dinescu et al. (2004) is a weighted mean of two measurements, one using galaxies and the other QSOs as standards of rest. The lensed QSO J0240 − 3434 is among the standards, and Dinescu et al. (2004) give individual values of the proper motion with respect to image A and B of the QSO. They are: $(\mu_\alpha, \mu_\delta) = (84 \pm 52, -4 \pm 64)$ mas century$^{-1}$ for image A and $(\mu_\alpha, \mu_\delta) = (73 \pm 34, -93 \pm 80)$ mas century$^{-1}$ for image B. Comparing these to our measurements in Table 3 shows an agreement within the uncertainties; however, because of the large uncertainties in the values above they do not provide a significant check on our results.

#### *5.4.1. Effect of Changing Charge Transfer Efficiency*

We have performed a parallel analysis that made no correction for the effects of charge transfer efficiency for each of the three fields. The resulting weighted mean $\mu_\alpha$ is nearly the same as the value in Table 3, but the mean $\mu_\delta$ is more negative by 17 mas century$^{-1}$. The $\chi^2$ around these means are 3.0 and 2.9, respectively, both for 3 degrees of freedom. These values are larger than those for the results in Table 3, demonstrating that correcting for the effects of the changing charge transfer efficiency significantly improves the agreement between the individual measurements of the proper motion.

### 5.5. Galactic Rest-Frame Proper Motion

The measured proper motion of the dSph contains contributions from the motion of the LSR and the peculiar motion of the Sun. The magnitude of each contribution depends on the location of the dSph in the sky. Removing them produces the Galactic rest-frame proper motion — the proper motion measured by a hypothetical observer at the location of the Sun but at rest with respect to the Galactic center. Columns (2) and (3) of Table 7 give the equatorial components, $(\mu_\alpha^{\rm Grf}, \mu_\delta^{\rm Grf})$, of the Galactic-rest-frame proper motion. Their derivation assumes: 220 km s$^{-1}$ for the circular velocity of the LSR; 8.5 kpc for the distance of the Sun from the Galactic center; and $(u_\odot, v_\odot, w_\odot) = (-10.00 \pm 0.36, 5.25 \pm 0.62, 7.17 \pm 0.38)$ km s$^{-1}$ (Dehnen & Binney 1998) for the peculiar velocity of the Sun, where the components are positive if $u_\odot$ points radially away from the Galactic center, $v_\odot$ is in the direction of rotation of the Galactic disk, and $w_\odot$ points in the direction of the north Galactic pole. Columns (4) and (5) give the Galactic rest-frame proper motion in the Galactic coordinate system, $(\mu_l^{\rm Grf}, \mu_b^{\rm Grf})$. Columns (6) - (8) give the $\Pi$, $\Theta$, and $Z$ components of the space velocity in a cylindrical coordinate system centered on the dSph. The components are positive if $\Pi$ points radially away from the Galactic axis of rotation, $\Theta$ points in the direction of rotation of the Galactic disk, and $Z$ points in the direction of the north Galactic pole. The derivation of these components assumes 138 kpc (Saviane et al. 2000) for the heliocentric distance to and $53.3 \pm 0.8$ km s$^{-1}$ (Walker et al. 2006) for the heliocentric radial velocity of Fornax. Columns (9) and (10) give the radial and tangential components of the space velocity for an observer at rest at the Galactic center. The component $V_r$ is positive if it points radially away from the Galactic center. The uncertainties in the listed quantities derive from Monte Carlo experiments. The bottom line in Table 7 gives the weighted mean of each listed quantity. Note that even though $\Pi^2 + \Theta^2 + Z^2 = V_r^2 + V_t^2$ for a measurement in a given field, this equality may not hold for the mean values.

The negative $V_r$ in Table 7 means that Fornax is moving towards the Milky Way. The negative value for $\Theta$ shows that the orbit is retrograde.

## 6. Orbit and Orbital Elements of Fornax

Knowing the space velocity of a dSph allows a determination of the orbit of the galaxy for a given form of the Galactic potential. This work adopts a Galactic potential that has a contribution from a disk of the form (Miyamoto & Nagai 1975)

$$\Psi_{\rm disk} = -\frac{GM_{\rm disk}}{\sqrt{R^2 + (a + \sqrt{Z^2 + b^2})^2}}, \tag{1}$$

from a spheroid of the form (Hernquist 1990)

$$\Psi_{\rm spher} = -\frac{GM_{\rm spher}}{R_{\rm GC} + c}, \tag{2}$$

and from a halo of the form

$$\Psi_{\rm halo} = v_{\rm halo}^2 \ln(R_{\rm GC}^2 + d^2). \tag{3}$$

In the above equations, $R_{\rm GC}$ is the Galactocentric distance, $R$ is the projection of $R_{\rm GC}$ onto the plane of the Galactic disk, and $Z$ is the distance from the plane of the disk. All other quantities in the equations are adjustable parameters and their values are the same as those adopted by Johnston et al. (1995): $M_{\rm disk} = 1.0 \times 10^{11}$ M$_\odot$, $M_{\rm spher} = 3.4 \times 10^{10}$ M$_\odot$, $v_{\rm halo} = 128$ km s$^{-1}$, $a = 6.5$ kpc, $b = 0.26$ kpc, $c = 0.7$ kpc, and $d = 12.0$ kpc.

Figure 26 shows the projections of the orbit of Fornax onto the $X$-$Y$ (*top left panel*), $X$-$Z$ (*bottom left panel*), and $Y$-$Z$ (*bottom right panel*) Cartesian planes. The orbit results from an integration of the motion in the Galactic potential given by equations (1)–(3). The integration extends for 6 Gyr backward in time and begins at the current location of Fornax with the negative of the space velocity components given in the bottom line of columns (6)–(8) of Table 7. The squares in Figure 26 mark the current location of the dSph, the stars indicate the center of the Galaxy, and the three small circles mark the points on the orbit at which $Z = 0$, or, in other words, where the orbit crosses the plane of the Galactic disk. The large circle is for reference; it has a radius of 30 kpc. In the right-handed coordinate system of Figure 26, the current location of the Sun is on the positive $X$-axis. The figure shows that Fornax is moving toward the Milky Way, is closer to apogalacticon than perigalacticon, and that it has a moderately polar orbit with a small eccentricity.

Table 8 tabulates the elements of the orbit of Fornax. The value of the quantity is in column (4) and its 95% confidence interval is in column (5). The latter comes from 1000 Monte Carlo experiments, where an experiment integrates the orbit using an initial velocity that is generated by randomly choosing the line-of-sight velocity and the two components of the measured proper motion from Gaussian distributions whose mean and standard deviation are the best estimate of the quantity and its quoted uncertainty, respectively. The eccentricity of the orbit is defined as

$$e = \frac{(R_a - R_p)}{(R_a + R_p)}. \tag{4}$$

The most likely orbit has about a 1.3:1 ratio of apogalacticon to perigalacticon, and the 95% confidence interval for the eccentricity allows ratios approximately between 1.2:1 and 2.2:1. The orbit is retrograde and only 11° away from being polar. The orbital period, 3.2 Gyr, is about 45% longer than that for Sculptor (2.2 Gyr; Piatek et al. (2006)) and more than a factor of two longer than those for Carina (1.4 Gyr; Piatek et al. (2003)) and Ursa Minor (1.5 Gyr; Piatek et al. (2005)).

## 7. Discussion

### 7.1. Is Fornax a Member of a Stream?

Lynden-Bell (1982) proposed that most, if not all, dSphs have a "tidal origin." In this picture, the tidal field of the Galaxy distorts a progenitor galaxy and creates streams of stars and gas which become gravitationally unbound to the progenitor galaxy, but move on a similar orbit. A new dSph forms from this material — tidal debris — when dissipation of energy makes distinct clumps of the debris gravitationally

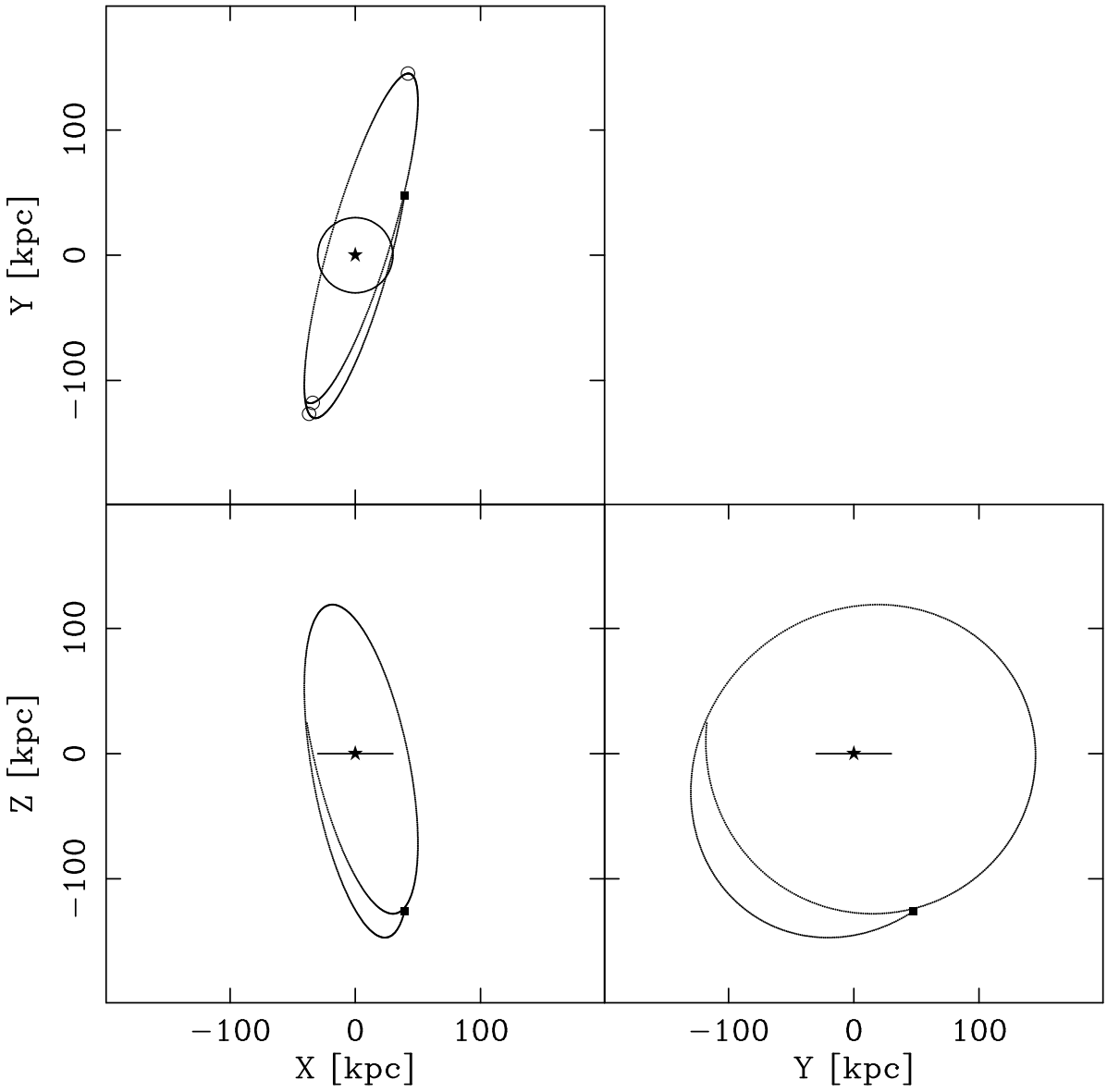


Fig. 26.— Projections of the orbit of Fornax on the $X$-$Y$ plane (*top left*), the $X$-$Z$ plane (*bottom left*), and the $Y$-$Z$ plane (*bottom right*). The origin of the right-handed coordinate system is at the Galactic center, which is marked with a star. The Galactic disk is in the $X$-$Y$ plane and the present location of the Sun is on the positive $X$ axis. The squares mark the current location of Fornax at $(X, Y, Z) = (39, 48, -126)$ kpc. For reference, the large circle in the $X$-$Y$ plane has radius of 30 kpc. The three small circles in the $X$-$Y$ projection mark the points at which Fornax passes through the plane of the Galactic disk. The integration starts from the present and extends backward in time for 6 Gyr.

bound. Consequently, the galaxies and globular clusters that formed from the debris move on similar orbits or, in other words, constitute a "stream." In the case of the "FLS" stream (Lynden-Bell 1982), Fornax is the surviving progenitor galaxy, whereas Leo I, Leo II, and Sculptor are the "condensate" dSphs. Lynden-Bell (1976) proposed that another great stream of galaxies is associated with the Magellanic Stream (Mathewson et al. 1974) and contains the Small and Large Magellanic Clouds, Draco, and Ursa Minor. The number of member galaxies in the streams increased as new satellite galaxies of the Milky Way were discovered. Majewski (1994) modified the FLS stream by including in it Sextans and renaming it as the "$FL^2S^2$" stream. The orbital plane of the $FL^2S^2$ stream is only slightly different from the original plane of the FLS stream. The idea of streams is verifiable. Given distances to and radial velocities of the members of a stream, the expected proper motions of the members can be calculated. Thus, in a more quantitative analysis, Lynden-Bell & Lynden-Bell (1995) calculated likelihoods for the existence of several streams containing dSphs and globular clusters and predicted the proper motions for the member galaxies and globular clusters. Fornax could be a member of one of four possible streams: streams 1a or 1b (together with Pal 14, Pal 15, and Eridanus), 4a (together with Sextans, Sculptor, and Pal 3), and 4b (together with Sextans and Sculptor). Table 9 contains the predicted motions for Fornax; columns (2) and (3) give the $\alpha$ and $\delta$ components of the proper motion, whereas columns (4) and (5) give this motion in polar coordinates. For easy comparison, the bottom line lists our measurement from Table 3.

The proper motion of Fornax predicted for stream 4a is in the closest agreement with our measurement, though even here the difference is more than 3.2 times the measurement uncertainty in one component. Given that there must be some uncertainty in the predicted motions, this difference may not be large enough to rule out membership in stream 4a. However, Piatek et al. (2006) ruled out the membership of Sculptor in stream 4a, so the reality of the stream hinges on the agreement between the predicted and actual proper motions of the remaining three members. Currently, neither Sextans nor Pal 3 has a measured proper motion.

### 7.2. Is the Orbit of Fornax in the Kroupa-Theis-Boily Plane?

Kroupa et al. (2005) noted that viewing 11 of the innermost dwarf galaxies, satellites of the Milky Way, from a point at infinity with $\ell = 167.^{\circ}91$ shows that the galaxies lie on nearly the same plane, whose poles are at $(\ell, b) = (168^{\circ}, -16^{\circ})$ and $(348^{\circ}, +16^{\circ})$. The probability is less than 0.5% that such an alignment of galaxies occurs by chance if the galaxies have an isotropic distribution of orbits. If the planar alignment is to persist in time, the dwarf galaxies must have orbits contained in this plane. Therefore, its persistence can be tested if proper motions of the galaxies are known.

Let the pole of an orbit be in the direction of the orbital angular momentum vector. Thus, the Galactic coordinates of the pole in terms of the orbital elements are:

$$(\ell, b) = (\Omega + 90^{\circ}, \Phi - 90^{\circ}). \tag{5}$$

For prograde orbits, $b < 0$, and for retrograde, $b > 0$. Using the best estimates for $\Omega$ and $\Phi$ from Table 8 and uncertainties that are 1-$\sigma$ errors from Monte Carlo simulations, the orbital pole of Fornax is at $(\ell, b) = (163^{\circ} \pm 8^{\circ}, 13^{\circ} \pm 4^{\circ})$. The poles of the orbit and plane are separated by $29.4^{\circ} \pm 4.1^{\circ}$. The separation is larger than the measurement uncertainties, however, the agreement between the two poles does not need to be exact because the plane has a finite thickness. Kroupa et al. (2005) find an rms distance from their plane of 26.4 kpc for the sample of 11 galaxies — which extends to about twice the distance of Fornax. This thickness is consistent with their claim of a ratio of height to radius of 0.15 for the disk. The tilt between the orbit of Fornax and the plane predicts that the time-averaged rms distance of Fornax from the plane is

47 kpc. This calculation assumes a circular orbit with a radius of 135 kpc, which is the average of the peri- and apogalacticons. We conclude that the orbit of Fornax is inconsistent with the plane. Whether the orbits of the dSphs are consistent with the predictions of Λ-CDM models for the Local Group will be addressed in a later article when measurements become available for Draco and Sextans.

### 7.3. What Happened to the Gas in Fornax?

Stetson et al. (1998) and Saviane et al. (2000) detected a population of blue and young main-sequence stars in Fornax. The stars are about $10^8$ years old and located in the central region of the galaxy. Quoting Stetson et al. (1998), the population "has a flattened distribution on the sky and its major axis is offset by roughly 30° from the symmetry axis of the galaxy as a whole." This detection implies that Fornax had to have HI $10^8$ years ago. However, a search for HI with the VLA by Young (1999) produced no detection at the limit of $4.6 \times 10^{18}$ cm$^{-2}$ at the galaxy center and $7.9 \times 10^{18}$ cm$^{-2}$ at the distance of one core radius from the center. Bouchard et al. (2006) searched for HI near the dwarf galaxies in the Local Group using the Parkes radio telescope. The survey confirmed the result of Young (1999) that there is no HI at the center of Fornax, but did identify gas offset about $30'$ north and west-northwest from the center. The strongest emission is between position angles of about 325° and 360° (see Figure 2 of Bouchard et al. 2006). The velocity of the gas is also offset — about 30 km s$^{-1}$ below that of the stars. Bouchard et al. (2006) calculate an approximately 10% probability that this gas is a chance superposition of a high-velocity cloud. This probability is not low enough to decisively establish a physical relationship between the gas and the galaxy. Bouchard et al. (2006) also note that subtracting the emission from the Milky Way is difficult for these observations. If there is no HI associated with Fornax, then why do young stars reside in the central region? If the HI is associated, why is it offset in both position and velocity?

Trying to answer such questions, Young (1999) offers two possibilities: (1) there is gas in the central region but it is either ionized or molecular or (2) HI was displaced from the central region in the past $10^8$ years. There are no published results of searches for HII or molecular gas, and so, (1) cannot be ignored or excluded until such results exist. In the case of (2), there must be a physical mechanism for displacing the gas. A supernova-driven wind blowing the gas from the center is one possible mechanism (Mac Low & Ferrara 1999). Ram pressure due to the motion of the galaxy through a gaseous halo of the Milky Way is another mechanism, *e.g.*, Gallart et al. (2001) or Mayer et al. (2006). In this case, the gas would trail the dSph and be displaced in the direction opposite to the Galactic rest-frame proper motion vector. This vector has a position angle of $120° \pm 8.5°$, *i.e.* pointing in the southeast direction, which would predict that the gas should be at a position angle of about 300°. However, the strongest HI emission has a position angle of about 340° and the elongation of the cloud is not aligned with the proper motion vector. Dinescu et al. (2004) propose a variation of the ram-pressure picture in which Fornax crossed the Magellanic plane — the plane containing the orbit of the LMC as defined by the space velocity from van der Marel et al. (2002) — about 190 Myr ago and passed through gas that was removed from the LMC but which still trails this gas-rich galaxy. This picture can be tested using our new proper motion for Fornax and a recently-measured proper motion for the LMC.

Kallivayalil et al. (2006a) measured the proper motion of the LMC using an observational technique similar to the one employed in this contribution. The measurement is based on *HST* observations of 21 QSOs in the direction of the LMC with the High Resolution Camera of the Advanced Camera for Surveys. The QSOs were discovered by their variability in the MACHO survey (Geha et al. 2003). The measured proper motion of the LMC is $(\mu_\alpha, \mu_\delta) = (203 \pm 8, 44 \pm 5)$ mas century$^{-1}$.

Integrating the two orbits backwards in time in the potential given by Eqs. 1–3 shows that Fornax crosses the orbital plane of the LMC about 1.4 Gyr ago and it does so at a distance of only 1.9 kpc from the orbit of the LMC. However, when Fornax is closest to the LMC orbit, the LMC will not arrive at that point for about another 0.8 Gyr. Numerical experiments that integrate the orbits using starting velocities with uncertainties determined by the observations indicate that Fornax crosses the plane of the LMC orbit between 0.80 Gyr and 2.0 Gyr ago with 95% confidence. Fornax approaches closer than 20 kpc to the orbit of the LMC in about 50% of the simulations. The Monte Carlo simulations show that the two galaxies do not come closer than 81 kpc at 97.5% confidence.

For the orbits adopted here, the recent loss of HI from Fornax 190 Myr ago cannot be attributed to the ram pressure from gas in the LMC orbital plane. The last crossing of the orbital plane by Fornax occurred about 1.4 Gyr ago, which is 1 Gyr before the cessation of star formation in the dSph. The plane crossing occurred 0.6 Gyr before the cessation of star formation with 97.5% confidence. Our conclusion differs from that of Dinescu et al. (2004) because of differences in the adopted orbits for Fornax and, particularly, the LMC.

Though an interaction between Fornax and gas from the LMC cannot explain the recent cessation of star formation in the dSph, the orbits of the two galaxies are likely to approach closely. It is still an open question whether this intersection of orbits has affected the star formation history or gas content of Fornax. The strongest argument against such an effect is that the closest approach of the two orbits occurs before the arrival of the LMC at that point. However, the amount of gas in the leading and trailing parts of the orbit are uncertain. The proper motion for the LMC of Kallivayalil et al. (2006a) implies a Galactocentric space velocity of 380 km $s^{-1}$, which yields an orbital period — calculated using the method in Section 6 — of 4.3 Gyr. This period is almost three times longer than that assumed in the canonical models for the formation of the Magellanic Stream (Gardiner 1999; Yoshizawa & Noguchi 2003; Conners et al. 2004). This conflict between the measured motion of the LMC and the models for the formation of the Magellanic Stream means that it is premature to rule out the removal of gas from Fornax by interaction with the Stream. An interaction with HI leading the LMC could have removed at least some gas from Fornax. Putman et al. (1998) identified what appears to be a leading tidal tail in HI maps. However, the likelihood of an interaction is decreased because the leading tail contains only about 25% as much gas as the trailing tail and the gas is organized in three disjoint complexes rather than in a continuous distribution (Brüns et al. 2005).

### 7.4. The Effect of the Galactic Tidal Force on the Structure of Fornax

If Fornax formed as a spherical system and if the Galactic tidal force has had an important effect on its structure, then the projected ellipticity would be the result of the stretching of the dSph in its orbital plane (*e.g.*, Johnston et al. 1995; Oh et al. 1995; Piatek & Pryor 1995). Thus, a nearly Galactocentric observer would see the Galactic rest-frame proper motion vector aligned with the projected major axis. From Table 1, the position angle of the major axis is $41^\circ \pm 1^\circ$, whereas this angle for the weighted mean Galactic rest-frame proper motion is $120^\circ \pm 8.5^\circ$. Within the uncertainties, these two angles are almost orthogonal to each other; in other words, the true major axis is not in the orbital plane.

Notwithstanding the disagreement in the two position angles above, the structure of Fornax exhibits several features which could have arisen as a consequence of tidal interaction with the Milky Way. Most recently, Coleman et al. (2005) show that: (1) the ellipticity of the isodensity contours increases with increasing semi-major axis, reaching a maximum at around $35'$, and then decreases beyond this radius; (2) the

position angle of ellipses fitted to the stellar surface density decreases with increasing semi-major axis; (3) isodensity contours on the eastern side of the galaxy are closer together than those on the western; and (4) the map of the stellar surface density shows stars of the dSph beyond the fitted tidal radius along the minor axis.

The feature which is most suggestive of a tidal interaction is (4). The direction of the Galactic rest-frame proper motion supports this picture; however, other aspects of the orbit do not: the large perigalacticon, long orbital period, small eccentricity, and approaching motion of the dSph do not favor the tidal origin for the observed "extratidal" stars. Coleman et al. (2005) propose that instead of the Galactic tidal force, a collision and merger event with another system is responsible for this observed feature.

### 7.5. Is There Dark Matter in Fornax?

Assuming that mass follows light and using the measured velocity dispersion, Mateo et al. (1991) derived a $M/L_V$ of $12.3 \pm 4.5$ in solar units for Fornax, noting that $M/L_V$s in the range between 5.3 and 26 are also possible given the uncertainties in the fitted structural parameters. The subsequent derivations of $M/L$ by Walcher et al. (2003) and Walker et al. (2006) are within this quoted range. Knowing the orbit of a dSph permits another approach to constraining its mass. The mass and orbit determine the tidal radius — the radius beyond which a star becomes unbound from the dSph due to gravitational interaction with the Milky Way. Making the assumption that the tidal radius is equal to the observed limiting radius then provides a value for the $M/L$. The value commonly adopted for the limiting radius is the limiting radius of a King (1966) model fitted to the radial surface brightness profile (unfortunately often also called the tidal radius). An exponential — which has no limiting radius — is also a good fit to the surface brightness profiles of dSphs, so the identification of the limiting radius determined from a King model with the tidal radius may be incorrect. Nevertheless, we calculate the $M/L$ of Fornax by equating the limiting and tidal radii. A constraint on the $M/L$ of a dSph with fewer assumptions, also given below, is that it must be large enough for the dSph to have survived the tidal interaction with the Milky Way given its measured orbit.

Equation (6) (King 1962; Oh et al. 1992) gives the tidal radius, $r_t$, as a function of the orbital elements of a dSph moving in a logarithmic potential for the Milky Way.

$$r_t = \left( \frac{(1-e)^2}{[(1+e)^2/2e] \ln[(1+e)/(1-e)] + 1} \frac{M}{M_G} \right)^{1/3} a. \tag{6}$$

In the equation, $e$ is eccentricity of the orbit, $a$ is the semi-major axis ($a \equiv (R_a + R_p)/2$), $M$ is the mass of the dSph, and $M_G$ is the mass of the Milky Way within $a$. Equating $r_t$ with the observed limiting radius derived by fitting a King (1966) model, $r_k$, gives a value for $M/L$ for a given orbit. Estimates of the limiting radius for Fornax range from $64'$ (Coleman et al. 2005) to $98'$ (Walcher et al. 2003). If $r_k = 64'$, then 10.4% of the orbits have $M/L_V > 5.3$ in 1000 Monte Carlo simulations similar to those that determined the uncertainties in the orbital elements; 0.2% of the orbits have $M/L_V > 26$. If $r_k = 98'$, then 100% of the orbits have $M/L_V > 5.3$ and 5.3% have $M/L_V > 26$. These results show that there is only a 5.3% chance that the global $M/L_V$ of Fornax is greater than 26 if the larger of the limiting radii is identified with the tidal radius. In other words, the orbit of Fornax is consistent with the broad range of $M/L$ values derived from virial equilibrium models and the observed limiting radius of the dSph and, thus, these calculations do not provide a strong constraint on the amount of dark matter in Fornax.

The average measured $M/L_V$ for Galactic globular clusters is 2.3 (Pryor & Meylan 1993). Could Fornax have a $M/L_V$ equal to this value and survive the effect of the Galactic tidal force until the present on our

derived orbit? Numerical simulations of tidal interactions by Oh et al. (1995) and Piatek & Pryor (1995) show that the ratio of the limiting radius derived by fitting a theoretical King model (King 1966), $r_k$, to the tidal radius defined by Equation (6) is a useful indicator of the importance of the Galactic tidal force on the structure of a dSph. These simulations show that: if $r_k/r_t \lesssim 1.0$, the Galactic tidal force has little effect on the structure of the dSph; at $r_k/r_t \approx 2.0$, the effect of the force increases rapidly with increasing $r_k/r_t$; and, for $r_k/r_t \approx 3.0$, the dSph disintegrates in a few orbits. Assuming that $M/L_V = 2.3$ and $r_k = 64'$, $r_k/r_t > 2.0$ for 0.3% of the orbits generated in Monte Carlo simulations. If $r_k = 98'$, the fraction is 10.8%. Thus, it is very likely that Fornax could have survived for a Hubble time on its current orbit while containing only luminous matter. We conclude that our orbit of Fornax and the observed limiting radius do not constrain the amount of dark matter in the dSph.

### 7.6. A Lower Limit for the Mass of the Milky Way

The space velocity of Fornax imposes a lower limit on the mass of the Milky Way, which is given by:

$$M = \frac{R(V_r^2 + V_t^2)}{2G}, \tag{7}$$

where $R$ is the Galactocentric distance, and $V_r$ and $V_t$ are the radial and tangential components of the space velocity, respectively, as measured by an observer at the center of the Galaxy. Equation 7 assumes a spherically symmetric mass distribution and 0 for the total energy of the satellite galaxy. Setting $R = 140$ kpc and using the values from Table 7 for $V_r$ and $V_t$, $M = (6.4 \pm 1.9) \times 10^{11} M_\odot$. This estimate does not place a strong constraint on the amount of mass within 140 kpc of the center of the Milky Way since the value is similar to the $5.4^{+0.1}_{-0.4} \times 10^{11} M_\odot$ within $R = 50$ kpc found by Sakamoto et al. (2003).

## 8. Summary

This contribution continues a series of articles, each reporting the proper motion of a dSph; here, we present a measurement for Fornax which replaces the value based on only part of the data in Piatek et al. (2002). The data come from imaging with the *HST* and STIS or PC2. Using the measured proper motion, we integrate the motion of the dSph to obtain its orbit and then discuss the proposed membership of Fornax in streams of satellites, the possible alignment of orbits of the Galactic satellites in a single plane, the association between HI and the dSph, the proposed interaction between the LMC and Fornax, the tidal interaction of the dSph with the Milky Way, the dark matter content of Fornax, and a lower limit on the mass of the Milky Way. The major findings are itemized below.

1. The weighted mean of the four independent measurements of the proper motion is $(\mu_\alpha, \mu_\delta) = (47.6 \pm 4.6, -36.0 \pm 4.1)$ mas century$^{-1}$ in the equatorial coordinate system for an observer at and moving with the Sun.

2. The Galactic rest-frame proper motion is that measured by an observer at the location of the Sun and at rest with respect to the Galactic center. In this system, the proper motion is $(\mu_\alpha^{\rm Grf}, \mu_\delta^{\rm Grf}) = (24.4 \pm 4.6, -14.3 \pm 4.1)$ mas century$^{-1}$.

3. The weighted means of the radial and tangential components of the space velocity with respect to a stationary observer at the Galactic center are $V_r = -31.8 \pm 1.7$ km s$^{-1}$ and $V_t = 196 \pm 29$ km s$^{-1}$, respectively. The negative sign of $V_r$ means that Fornax is approaching the Milky Way.

4. The orbit resulting from the integration of the best estimate of the motion in a realistic potential of the Milky Way shows that Fornax is approaching a perigalacticon of 118 kpc on an approximately polar orbit with an eccentricity of 0.13. The apogalacticon of the orbit is 152 kpc and the orbital period is 3.2 Gyr.

5. Fornax is not a member of stream 1a, 1b, or 4b of Lynden-Bell & Lynden-Bell (1995), though it could be a member of stream 4a. Since Piatek et al. (2005) ruled out the membership of the Sculptor dSph in stream 4a, the reality of this stream depends on whether the proper motions of the other proposed members, which still need to be measured, agree with the predictions.

6. The orbit of Fornax is not in the Kroupa-Theis-Boily plane, which contains eleven of the Galactic satellite galaxies.

7. Our findings do not support the hypothesis of Dinescu et al. (2004) that Fornax lost its HI about 200 Myr ago as it passed through the stream of gas trailing the LMC in its orbit. Our proper motion for Fornax and that of Kallivayalil et al. (2006a) for the LMC show that Fornax approaches within about 1.9 kpc of the orbit of the LMC, but 1.4 Gyr ago and 0.8 Gyr before the LMC arrives at that point. An interaction 1.4 Gyr ago does not explain why star formation in Fornax continued until 200 Myr ago, though uncertainties in modeling the Magellanic Stream keep this mechanism for the loss of HI from Fornax from being definitively ruled out.

CP and SP acknowledge the financial support of the Space Telescope Science Institute through the grants HST-GO-07341.03-A and HST-GO-08286.03-A and of the National Science Foundation through grant AST-0098650. EWO acknowledges support from the Space Telescope Science Institute through the grants HST-GO-07341.01-A and HST-GO-08286.01-A and from the National Science Foundation through the grants AST-0205790 and AST-0507511. MM acknowledges support from the Space Telescope Science Institute through the grants HST-GO-07341.02-A and HST-GO-08286.02-A and from the National Science Foundation through the grant AST-0098661. DM is supported by FONDAP Center for Astrophysics 15010003 and by a Fellowship from the John Simon Guggenheim Foundation.

## REFERENCES

Anderson, J., & King, I. R. 1999, PASP, 111, 1095

Anderson, J., & King, I. R. 2000, PASP, 112, 1360

Anderson, J., & King, I. R. 2003, PASP, 115, 113

Anguita, C., Loyola, P., & Pedreros, M. H. 2000, AJ, 120, 845

Bristow, P., & Alexov, A. 2002, CE-STIS-ISR 2002-001

Bristow, P., Piatek, S., & Pryor, C. 2005, ST-ECF Newsletter, 38, 12

Brown, T., et al., 2002, in *HST* STIS Data Handbook Version 4.0, ed. B. Mobasher (Baltimore: STScI)

Brüns, C., et al., 2005, A& A, 432, 45

Brunthaler, A., Reid, M. J., Falcke, H., Greenhill, L. J., & Henkel, C. 2005, Sci., 307, 1440

Bouchard, A., Carignan, C., & Staveley-Smith, L. 2006, AJ, 131, 2913

Buonanno, R., Corsi, C. E., Castellani, M., Marconi, G., Fusi Pecci, F., & Zinn, R. 1999, AJ, 118, 1671

Coleman, M. G., Da Costa, G. S., Bland-Hawthorn, J., & Freeman, K. 2005, AJ, 129, 1443

Coleman, M., Da Costa, G. S., Bland-Hawthorn, J., Martinez-Delgado, D., Freeman, K. C., & Malin, D. 2004, AJ, 127, 832

Conners, T. W., Kawata, D., Maddison, S. T., & Gibson, B. K. 2004, PASA, 21, 222

Dehnen, W., & Binney, J. J. 1998, MNRAS, 298, 387

Demers, S., Irwin, M. J., & Kunkel, W. E. 1994, AJ, 108, 1648

Dinescu, D. I., Girard, T. M., van Altena, W. F., & Lopez, C. E. 2005, ApJ, 618, L25

Dinescu, D. I., Keeney, B. A., Majewski, S. R., & Girard, T. M. 2004, 128, 687

Dinescu, D. I., Martinez-Delgado, D., Girard, T. M., Penarrubia, J., Rix, H.-W., Butler, D., & van Altena, W. F. 2005, ApJ, 631, L49

Drake, A. J., Cook, K. H., Alcock, C., Axelrod, T. S., Geha, M., & MACHO Collaboration 2001, BAAS, 33, 1379

Gallart, C., Martínez-Delgado, D., Gómez-Flechoso, M. A., & Mateo, M. 2001, AJ, 121, 2572

Gardiner, L. T. 1999, Stromlo Workshop on High-Velocity Clouds, ed. B. K. Gibson & M. E. Putman, ASP Conf. Ser. 166, 292

Geha, M., et al. 2003, AJ, 125, 1

Gill, S. P. D., Knebe, A., Gibson, B. K., & Dopita, M. A. 2004, MNRAS, 351, 410

Goudfrooij, P., Maíz-Apellániz, J., Brown, T., & Kimble, R. 2006, STIS ISR 2006-01

Hernquist, L. 1990, ApJ, 356, 359

Heyer, B., et al. 2004, WFPC2 Instrument Handbook, Ver. 9.0 (Baltimore: STScI)

Irwin, M. J., Demers, S., & Kunkel, W. E. 1996, BAAS, 28, 932

Irwin, M. & Hatzidimitriou, D. 1995, MNRAS, 277, 1354

Janesick, J. R., Soli, G., Elliot, T. S., & Collins, S. A. 1991, Proc. SPIE, 1447, 87

Johnston, K. V., Spergel, D. N., & Hernquist, L. 1995, ApJ, 451, 598

Jones, B. F., Klemola, A. R., & Lin, D. N. C. 1994, AJ, 107, 1333

Kallivayalil, N., van der Marel, R. P., Alcock, C., Axelrod, T., Cook, K. H., Drake, A. J., & Geha, M. 2006, ApJ, 638, 772

Kallivayalil, N., van der Marel, R. P., & Alcock, C. 2006, ApJ submitted (astro-ph/0606240)

King, I. 1962, AJ, 67, 471

King, I. 1966, AJ, 71, 64

Kroupa, P. & Bastian, U. 1997, New Astr., 2, 77

Kroupa, P., Roser, S., & Bastian, U. 1994, MNRAS, 266, 412

Kroupa, P., Theis, C., & Boily, C. M. 2005, A&A, 431, 517

Libeskind, N. I., Frenk, C. S., Cole, S., Helly, J. C., Jenkins, A., Navarro, J. F., & Power, C. 2005, MNRAS, 363, 146

Lynden-Bell, D. 1976, MNRAS, 174, 695

Lynden-Bell, D. 1982, Observatory, 102, 202

Lynden-Bell, D., & Lynden-Bell, R. M. 1995, MNRAS, 275, 429

Mac Low, M.-M., & Ferrara, A. 1999, ApJ, 513, 142

Majewski, S. R. 1994, ApJ, 431, L17

Mateo, M. 1998, ARA&A, 36, 435

Mateo, M., Olszewski, E., Welch, D. L., Fischer, P., & Kunkel, W. 1991, AJ, 102, 914

Mathewson, D. S., Cleary, M. N., & Murray, J. D. 1974, ApJ, 190, 291

Mayer, L., Mastropietro, C., Wadsley, J., Stadel, J., & Moore, B. 2006, MNRAS, 369, 1021

Miyamoto, M., & Nagai R. 1975, PASJ, 27, 533

Moore, B., Diemand, J., Madau, P., Zemp, M., & Stadel, J. 2006, MNRAS, 368, 563

Oh, K. S., Lin, D. N. C., & Aarseth, S. J. 1992, ApJ, 386, 506

Oh, K. S., Lin, D. N. C., & Aarseth, S. J. ApJ, 442, 142

Olszewski, E. W., Mateo, M., Harris, J., Walker, M. G., Coleman, M. G. & Da Costa, G. S. 2006, AJ, 131, 912

Pedreros, M. H., Anguita, C., & Maza, J. 2002, AJ, 123, 1971

Piatek, S., & Pryor, C. 1995, AJ, 109, 1071

Piatek, S., Pryor, C., Olszewski, E. W., Harris, H. C., Mateo, M., Minniti, D., Monet, D. G., Morrison, H., & Tinney, C G. 2002, AJ, 124, 3198

Piatek, S., Pryor, C., Olszewski, E. W., Harris, H. C., Mateo, M., Minniti, D., & Tinney, C. G. 2003, AJ, 126, 2346

Piatek, S., Pryor, C., Bristow, P., Olszewski, E. W., Harris, H. C., Mateo, M., Minniti, D., & Tinney, C. G. 2005, AJ, 130, 95

Piatek, S., Pryor, C., Bristow, P., Olszewski, E. W., Harris, H. C., Mateo, M., Minniti, D., & Tinney, C. G. 2006, AJ, 131, 1445

Pryor, C., & Meylan, G. 1993, in Structure and Dynamics of Globular Clusters, edited by S. Djorgovski & G. Meylan (ASP, San Francisco), p. 357

Putman, M. E., et al., 1998, Nature, 394, 752

Sakamoto, T., Chiba, M., & Beers, T. C. 2003, A&A, 397, 899

Saviane, I., Held, E. V., & Bertelli, G. 2000, A&A, 355, 56

Scholtz, R.-D., & Irwin, M. J. 1993, in IAU Symp. 161, Astronomy from Wide-Field Imaging, ed. H. T. MacGillivray et al. (Dordrecht: Kluwer), 535

Schweitzer, A. E., Cudworth, K. M., & Majewski, S. R. 1997, in ASP Conf. Ser. 127, Proper Motions and Galactic Astronomy, ed. R. M. Humphreys (San Francisco: ASP), 132

Schweitzer, A. E., Cudworth, K. M., Majewski, S. R., & Suntzeff, N. B. 1995, AJ, 110, 2747

Shaklan, S., Sharman, M. C., & Pravdo, S. H. 1995, Appl. Opt., 34, 6672

Shapley, H. 1938a, Harv. Obs. Bull., 908, 1

Shapley H., 1938b, Nature, 142, 715

Stetson, P. B. 1987, PASP, 99, 191

Stetson, P. B. 1992, in ASP Conf. Ser. Vol. 25, Astronomical Data Analysis Software and Systems, ed. D. M. Worrall, C. Biemesderfer, & J. Barnes (San Francisco: ASP), 297

Stetson, P. B. 1994, PASP, 106, 250

Stetson, P. B., Hesser, J. E., & Smecker-Hane, T. A. 1998, PASP, 110, 533

Tinney, C. G. 1995, MNRAS, 277, 609

Tinney, C. G, Da Costa, G. S., & Zinnecker, H. 1997, MNRAS, 285, 111

van den Bergh, S. 1999, A&A Rev., 9, 273

van den Bergh, S. 2000, The Galaxies of the Local Group (Cambridge: Cambridge Univ. Press)

van der Marel, R. P., Alves, D. R., Hardy, E., & Suntzeff, N. B. 2002, AJ, 124, 2639

Walcher, C. J., Fried, J. W., Burkert, A., & Klessen, R. S. 2003, A&A, 406, 847

Walker, M. G., Mateo. M., Olszewski, E. W., Bernstein, R. A., Wang, X., & Woodroofe, M. 2006, AJ, 131, 2114

Whitmore, B., Heyer, I., & Casertano, S. 1999, PASP, 111, 1559

Yentis, D. J. et al. 1992, in MacGillivray H., Thomson E., eds, Digitized Optical Sky Surveys. Kluwer, Dordrecht, p. 67

Yoshizawa, A. M., & Noguchi, M. 2003, MNRAS, 339, 1135.

Young, L. M. 1999, 117, 1758

Zentner, A. R., Kravtsov, A. V., Gnedin, O. Y., & Klypin, A. A. 2005, ApJ, 629, 219

Zhao, H. 1998, ApJ Letters, 500, L149

This preprint was prepared with the AAS LaTeX macros v5.2.

Table 1. Fornax at a Glance

| Quantity (1) | Value (2) | Reference (3) |
|---|---|---|
| Right Ascension, $\alpha$ (J2000.0) | $02:39:53.1$ | van den Bergh (1999 ) |
| Declination, $\delta$ (J2000.0) | $-34:30:16.0$ | van den Bergh (1999) |
| Galactic longitude, $\ell$ | $237.245^\circ$ | |
| Galactic latitude, $b$ | $-65.663^\circ$ | |
| Heliocentric distance | $138 \pm 8$ kpc | Saviane et al. (2000) |
| Luminosity, $L_V$ | $(1.4 \pm 0.4) \times 10^7\ L_\odot$ | Irwin & Hatzidimitriou (1995) |
| Ellipticity, $e$ | $0.30 \pm 0.01$ | $''$ |
| Position angle | $41^\circ \pm 1^\circ$ | $''$ |
| Core radius | $13.7' \pm 1.2'$ | $''$ |
| Tidal radius | $71.1' \pm 4.0'$ | $''$ |
| Heliocentric radial velocity | $53.3 \pm 0.8$ km s$^{-1}$ | Walker et al. (2006) |

Table 2. Fornax: Information about Fields and Images

| Field (1) | R.A. (J2000.0) (2) | Decl. (J2000.0) (3) | Date $yyyy-mm-dd$ (4) | Detector (5) | Filter (6) | $T_{exp}$[a] (s) (7) |
|---|---|---|---|---|---|---|
| FOR J0240 − 3434 | 02 40 07.70 | −34 34 20.01 | 1999 − 03 − 10 | PC2 | F606W | 18 × 160 |
| | | | 2001 − 03 − 08 | | | 16 × 160 |
| | | | 2003 − 03 − 08 | | | 16 × 160 |
| FOR J0240 − 3438 | 02 40 38.70 | −34 38 58.00 | 2000 − 01 − 31 | STIS | 50CCD | 24 × 192 |
| | | | 2001 − 01 − 25 | | | 24 × 192 |
| | | | 2002 − 01 − 29 | | | 24 × 192 |
| FOR J0238 − 3443 | 02 38 43.80 | −34 43 53.00 | 2000 − 03 − 08 | STIS | 50CCD | 24 × 193 |
| | | | 2001 − 03 − 08 | | | 24 × 192 |
| | | | 2003 − 03 − 09 | | | 24 × 192 |

[a]Number of images times the mean exposure time. The actual exposure times of individual images may differ by a few percent from the mean due to constraints imposed by the orbit of HST.

Table 3. Measured Proper Motion of Fornax

| Field (1) | $\mu_\alpha$ (mas century$^{-1}$) (2) | $\mu_\delta$ (mas century$^{-1}$) (3) |
|---|---|---|
| FOR J0240 − 3434$A$ | $54.1 \pm 8.5$ | $-27.5 \pm 7.1$ |
| FOR J0240 − 3434$B$ | $42.4 \pm 9.6$ | $-47.7 \pm 10.9$ |
| FOR J0240 − 3438 | $53.6 \pm 15.8$ | $-32.5 \pm 16.2$ |
| FOR J0238 − 3443 | $44.6 \pm 7.2$ | $-39.1 \pm 6.0$ |
| Weighted mean | $47.6 \pm 4.6$ | $-36.0 \pm 4.1$ |

Table 4. Measured Proper Motions For Objects in the FOR J0240 − 3434 Field

| ID (1) | X (pixels) (2) | Y (pixels) (3) | $S/N$ (4) | $\mu_\alpha$ (mas century$^{-1}$) (5) | $\mu_\delta$ (mas century$^{-1}$) (6) | $\chi^2$ (7) |
|---|---|---|---|---|---|---|
| 1 | 458 | 461 | 163 | $0 \pm 10$ | $0 \pm 8$ | 1.47 |
| 2 | 562 | 540 | 122 | $0 \pm 11$ | $0 \pm 11$ | 1.37 |
| 3 | 162 | 463 | 60 | $6 \pm 9$ | $-28 \pm 12$ | 1.44 |

Table 5. Measured Proper Motions For Objects in the FOR J0240 − 34348 Field

| ID (1) | X (pixels) (2) | Y (pixels) (3) | $S/N$ (4) | $\mu_\alpha$ (mas century$^{-1}$) (5) | $\mu_\delta$ (mas century$^{-1}$) (6) | $\chi^2$ (7) |
|---|---|---|---|---|---|---|
| 1 | 480 | 520 | 218 | $0 \pm 16$ | $0 \pm 16$ | 0.98 |
| 2 | 781 | 960 | 24 | $116 \pm 34$ | $24 \pm 27$ | 0.81 |
| 3 | 126 | 358 | 15 | $442 \pm 54$ | $-317 \pm 47$ | 0.31 |

Table 6. Measured Proper Motions For Objects in the FOR J0238 − 3443 Field

| ID (1) | X (pixels) (2) | Y (pixels) (3) | $S/N$ (4) | $\mu_\alpha$ (mas century$^{-1}$) (5) | $\mu_\delta$ (mas century$^{-1}$) (6) | $\chi^2$ (7) |
|---|---|---|---|---|---|---|
| 1 | 499 | 541 | 167 | $0 \pm 8$ | $0 \pm 7$ | 0.33 |
| 2 | 739 | 874 | 135 | $48 \pm 10$ | $-80 \pm 12$ | 2.65 |
| 3 | 905 | 278 | 111 | $4 \pm 8$ | $-29 \pm 9$ | 0.48 |
| 4 | 719 | 833 | 104 | $28 \pm 9$ | $-63 \pm 12$ | 1.24 |
| 5 | 955 | 996 | 27 | $52 \pm 21$ | $-143 \pm 22$ | 4.24 |
| 6 | 708 | 995 | 10 | $113 \pm 61$ | $-226 \pm 40$ | 3.15 |

Table 7. Galactic-Rest-Frame Proper Motion and Space Velocity of Fornax

| Field (1) | $\mu_\alpha^{\rm Grf}$ (mas cent$^{-1}$) (2) | $\mu_\delta^{\rm Grf}$ (3) | $\mu_l^{\rm Grf}$ (mas cent$^{-1}$) (4) | $\mu_b^{\rm Grf}$ (5) | $\Pi$ (km s$^{-1}$) (6) | $\Theta$ (km s$^{-1}$) (7) | $Z$ (km s$^{-1}$) (8) | $V_r$ (km s$^{-1}$) (9) | $V_t$ (km s$^{-1}$) (10) |
|---|---|---|---|---|---|---|---|---|---|
| FOR J0240 − 3434$A$ | $30.9 \pm 8.5$ | $-5.8 \pm 7.1$ | $0.2 \pm 7.2$ | $31.4 \pm 8.5$ | $172 \pm 51$ | $-21 \pm 47$ | $116 \pm 23$ | $-27.7 \pm 3.1$ | $206 \pm 54$ |
| FOR J0240 − 3434$B$ | $19.2 \pm 9.6$ | $-26.0 \pm 10.8$ | $22.1 \pm 10.8$ | $23.5 \pm 9.6$ | $109 \pm 57$ | $-158 \pm 71$ | $94 \pm 26$ | $-36.6 \pm 4.1$ | $211 \pm 66$ |
| FOR J0240 − 3438 | $30.4 \pm 15.8$ | $-10.8 \pm 16.2$ | $5.2 \pm 16.2$ | $31.8 \pm 15.8$ | $170 \pm 94$ | $-54 \pm 110$ | $118 \pm 43$ | $-29.8 \pm 6.2$ | $212 \pm 96$ |
| FOR J0238 − 3443 | $21.4 \pm 7.2$ | $-17.3 \pm 6.0$ | $12.9 \pm 6.1$ | $24.3 \pm 7.2$ | $121 \pm 43$ | $-100 \pm 39$ | $96 \pm 19$ | $-33.1 \pm 2.7$ | $180 \pm 44$ |
| Weighted mean | $24.4 \pm 4.6$ | $-14.3 \pm 4.1$ | $9.6 \pm 4.1$ | $26.8 \pm 4.6$ | $137 \pm 27$ | $-80 \pm 27$ | $103 \pm 12$ | $-31.8 \pm 1.7$ | $196 \pm 29$ |

Table 8. Orbital elements of Fornax

| Quantity (1) | Symbol (2) | Unit (3) | Value (4) | 95% Conf. Interv. (5) |
|---|---|---|---|---|
| Perigalacticon | $R_p$ | kpc | 118 | $(66, 137)$ |
| Apogalacticon | $R_a$ | kpc | 152 | $(144, 242)$ |
| Eccentricity | $e$ | | 0.13 | $(0.11, 0.38)$ |
| Period | $T$ | Gyr | 3.2 | $(2.5, 4.6)$ |
| Inclination | $\Phi$ | deg | 101 | $(94, 107)$ |
| Longitude | $\Omega$ | deg | 73 | $(58, 90)$ |

Table 9. Predicted Proper Motion of Fornax

| Stream No. (1) | $\mu_\alpha$ (mas century$^{-1}$) (2) | $\mu_\delta$ (mas century$^{-1}$) (3) | $\lvert\mu\rvert$ (mas century$^{-1}$) (4) | PA (deg) (5) |
|---|---|---|---|---|
| 1a | 30 | –15 | 34 | 117 |
| 1b | 15 | –27 | 31 | 151 |
| 4a | 38 | –23 | 44 | 121 |
| 4b | 6.3 | –19 | 20 | 162 |
| Our Result | $47.6 \pm 4.6$ | $-36.0 \pm 4.1$ | $60.0 \pm 4.4$ | $127 \pm 4.1$ |